

Exploring over 700 massive quiescent galaxies at $z = 2-7$: Demographics and stellar mass functions

William M. Baker^{1,*}, Francesco Valentino^{2,3}, Claudia del P. Lagos^{4,5,2}, Kei Ito^{2,3}, Christian Kragh Jespersen⁶, Rashmi Gottumukkala^{2,7}, Jens Hjorth¹, Danial Langeroodi¹, and Aidan Sedgewick¹

¹ DARK, Niels Bohr Institute, University of Copenhagen, Jagtvej 155A, DK-2200 Copenhagen, Denmark

² Cosmic Dawn Center (DAWN), Copenhagen, Denmark

³ DTU Space, Technical University of Denmark, Elektrovej 327, DK- 2800 Kgs. Lyngby, Denmark

⁴ International Centre for Radio Astronomy Research (ICRAR), M468, University of Western Australia, 35 Stirling Hwy, Crawley, WA 6009, Australia

⁵ ARC Centre of Excellence for All Sky Astrophysics in 3 Dimensions (ASTRO 3D)

⁶ Department of Astrophysical Sciences, Princeton University, Princeton, NJ 08544, USA

⁷ Niels Bohr Institute, University of Copenhagen, Jagtvej 128, 2200 Copenhagen N, Denmark

June 5, 2025

ABSTRACT

High-redshift ($z > 2$) massive quiescent galaxies are crucial tests of early galaxy formation and evolutionary mechanisms through their cosmic number densities and stellar mass functions (SMFs). We explore a sample of 745 massive ($M_* > 10^{9.5} M_\odot$) quiescent galaxies from $z = 2 - 7$ in over 800 arcmin² of NIRC*m* imaging from a compilation of public JWST fields (with a total area $> 5 \times$ previous JWST studies). We compute and report their cosmic number densities, stellar mass functions, and cosmic stellar mass density. We confirm a significant overabundance of massive quiescent galaxies relative to a range of cosmological hydrodynamical simulations and semi-analytic models (SAMs). We find that one SAM, SHARK is able to reproduce our observed number density with the addition of mock observational errors, but that it is still unable to produce quiescent galaxies of the same masses. We find that no simulations or SAMs accurately reproduce the SMF for massive quiescent galaxies at any redshift within the interval $z = 2 - 5$. This shows that none of these models' feedback prescriptions are fully capturing high- z galaxy quenching, challenging the standard formation scenarios. We find a greater abundance of lower-mass ($M_* < 10^{10} M_\odot$) quiescent galaxies than previously found, highlighting the importance of sSFR cuts rather than simple colour selection. We show the importance of this selection bias, alongside individual field-to-field variations caused by cosmic variance, in varying the observed quiescent galaxy SMF, especially at higher- z . We also find a steeper increase in the cosmic stellar mass density for massive quiescent galaxies than has been seen previously, with an increase of around a factor of 60 from $z = 4.5$ to $z = 2$, indicating the increasing importance of galaxy quenching within these epochs.

Key words. Galaxies: high-redshift, Galaxies: evolution, Galaxies: formation, Galaxies: star-formation, Galaxies: elliptical and lenticular, cD,

1. Introduction

Massive quiescent galaxies are crucial tests of our understanding of early galaxy formation and evolutionary mechanisms. Simply "counting" their number within a given volume (i.e. computing their cosmic number densities) has strong implications as to the strength and effect of feedback processes on galaxy evolution (e.g. Somerville & Davé 2015; Beckmann et al. 2017; Merlin et al. 2019; Donnari et al. 2021a,b; Baker et al. 2025b; De Lucia et al. 2024; Lagos et al. 2025).

These massive quiescent galaxies are the descendents of earlier star-forming galaxies that have undergone the process of quenching, after which galaxies cease forming new stars (at least in any significant number) (for a review see Man & Belli 2018; Curtis-Lake et al. 2023; De Lucia et al. 2025).

Many possible quenching mechanisms have been proposed such as stellar feedback (Larson 1974; Dekel & Silk 1986; Veilleux et al. 2005), AGN feedback (Silk & Rees 1998; Croton et al. 2006; Fabian 2012), starvation (Peng et al. 2015; Trusler et al. 2020; Baker et al. 2024), morphological (Martig et al.

2009), cosmic rays, environmental, and many more (Man & Belli 2018). It is often helpful to split quenching mechanisms based on the stellar masses of the galaxies in question. This becomes even more important when investigating high-redshift galaxy quenching as it necessarily places more constraints on the masses of galaxies due to the younger age of the Universe at these redshifts.

At least more locally, galaxy quenching has been shown to be roughly split into two categories based on stellar mass and environment (Peng et al. 2010), mostly corresponding to internal versus external quenching mechanisms (also seen in simulations Lim et al. 2025). The external mechanisms (under the broad name of environmental quenching) correspond to the region in which the galaxy is present, with more overdense regions having a greater proportion of passive galaxies found (Dressler 1980). This is traditionally thought to affect lower mass galaxies ($M_* < 10^{10} M_\odot$) more than the high-mass ($M_* > 10^{10} M_\odot$) due to their shallower gravitational potentials making them less able to hold on to their gas reservoirs, whilst dealing with processes such as ram-pressure stripping or harassment (Gunn & Gott 1972; Peng et al. 2010). For more massive galaxies, gener-

* william.baker@nbi.ku.dk

ally internal quenching mechanisms are thought to be the most important, especially in cosmological simulations (see for a review Somerville & Davé 2015; Man & Belli 2018; Vogelsberger et al. 2020, but mergers and environment can still play a role in certain cases).

Since the advent of the JWST we have been finding many more high- z massive quiescent galaxies than previously found, and to even higher redshifts (e.g. Carnall et al. 2024; Nanayakkara et al. 2025, 2024; Baker et al. 2025b; de Graaff et al. 2025; Weibel et al. 2024a; Wu 2025). This has resulted in high densities that disagree with many aspects of theory (Schreiber et al. 2018; Merlin et al. 2019; Carnall et al. 2023a; Valentino et al. 2023; Baker et al. 2025b). This was shown in some of the first data taken with JWST (e.g. Carnall et al. 2023a; Long et al. 2024; Russell et al. 2024; Alberts et al. 2024), but, due to the small regions probed, cosmic variance was shown to be an increasingly important factor (Valentino et al. 2023). Compared to theory, it is also important to take into account the effects of cosmic variance within cosmological simulations as in Baker et al. (2025b), where they found that although this affects number densities, there is still a 3σ disagreement at $z>3$. The observational overabundance remains even when using spectroscopy to better ensure the fidelity of the quiescent galaxy sample (Baker et al. 2025b). This has resulted in the general consensus that we are observing more of these high- z quiescent galaxies than we find in our best cosmological simulations (Valentino et al. 2023; Lagos et al. 2025).

However, the masses probed are also important; the JWST has uncovered a population of low-mass ($M_\star < 10^{9.0} M_\odot$) "mini" or "rapidly" quenched galaxies at $z>5$ (Strait et al. 2023; Looser et al. 2024; Baker et al. 2025a). These galaxies do not fulfil the traditional criteria of quiescent galaxies as whilst they have visible Balmer breaks, they also have low masses ($M_\star \leq 10^9 M_\odot$) and very blue colours, an indication of very recent quenching $t_{\text{quench}} \leq 30\text{Myr}$. We will not explore these types of galaxies in this paper (we refer interested readers to one of the following works Looser et al. 2024; Baker et al. 2025a; Gelli et al. 2025; Dome et al. 2024).

If we classify high- z massive quiescent galaxies as those with stellar masses above $M_\star > 10^{9.5} M_\odot$, then when comparing to cosmological hydrodynamical simulations and semi-analytic models (SAMs), another key aspect to probe is not only the number densities, but also the number of quiescent galaxies of a given stellar mass within a given area. This gives the well-studied stellar mass function (Grazian et al. 2015; Davidzon et al. 2017; Leja et al. 2020; Weaver et al. 2023; Weibel et al. 2024b), only for high- z quiescent galaxies. The stellar mass function is crucial for understanding many aspects of galaxy evolution. However, high- z exploration of the SMF has previously been conducted based on colour selection, rather than full Bayesian SED modelling (e.g. Weaver et al. 2023). As has previously been shown in multiple works from both observations and simulations, this is likely to miss a significant number of quiescent galaxies at high- z (Antwi-Danso et al. 2023; Lovell et al. 2023; Baker et al. 2025b). Generally cosmological hydrodynamical simulations and SAMs are designed to reproduce the stellar mass function at low redshifts, but at high- z predictions deviate substantially for massive quiescent galaxies (Lagos et al. 2025) compared to previous observations (Weaver et al. 2023). The different predictions for high- z -number densities and stellar mass functions from various cosmological simulations and SAMs were explored in depth in Lagos et al. (2025). They showed that there were significant differences between the observations and simulations, as well as significant differences between the simulations and SAMs them-

selves. This opens up an exciting new avenue for testing our understanding of galaxy evolutionary physics using the abundances and masses of high- z quiescent galaxies.

However, on the observational side, we have yet to fully exploit the wide area of publicly available JWST imaging, the largest area explored so far being 145 arcmin² in Valentino et al. (2023). Currently we have one spectroscopically confirmed quiescent galaxy above $z = 5$ (Weibel et al. 2024a; Valentino et al. 2025) and a handful above $z=4$ (Tanaka et al. 2019; Carnall et al. 2023b, 2024; Kakimoto et al. 2024; Urbano Stawinski et al. 2024; de Graaff et al. 2025; Baker et al. 2025b; Barrufet et al. 2025; Wu 2025; Nanayakkara et al. 2025; Antwi-Danso et al. 2025). To properly compute number densities we require a comprehensive understanding of the area probed, which is complex in the case of spectroscopy due to target selection. For this we require a photometric approach which also brings the benefit of greatly enhanced sample sizes, albeit without the exquisite detail of a spectrum.

In this paper, we will explore a comprehensive photometric sample of high- z quiescent galaxies above $z=2$. We will compute their cosmological number densities, stellar mass functions, and report high- z candidates. Our combined area consists of 816 arcmin² of publicly available JWST imaging, which is more than $5\times$ larger than Valentino et al. (2023).

2. Data

As we want to compute number densities and stellar mass functions, it is crucial that we probe a large area of JWST imaging. To do this, we use a combination of publicly available JWST fields. We use the Cosmic Epochs Early Release Survey (CEERS, DDERS 1345 Finkelstein et al. 2025), Public Release IMaging for Extragalactic Research (PRIMER, GO 1837 Dunlop et al. 2021; Donnan et al. 2024), and the JWST Advanced Deep Extragalactic Survey (JADES, GTO 1180, 1181, 1210, 1287, 1215 Eisenstein et al. 2023b; Rieke et al. 2023). This consists of multiband imaging in EGS, UDS, COSMOS, GOODS-S and GOODS-N (Giavalisco et al. 2004; Grogin et al. 2011; Koekemoer et al. 2011). The idea behind this is that we are more robust to cosmic variance using a combination of different fields from different regions of the sky. This culminates in a combined total area of 816.9 cMpc³. We use the photometric data from the DJA (Valentino et al. 2023; Heintz et al. 2025)¹ which was processed with GRIZLI (Brammer 2023). See Valentino et al. (2023) for more details about the data reduction and photometric extraction process.

For our colour selection with EAZY (Brammer et al. 2008) we use all available photometric data. For SED modelling with BAGPIPES (Carnall et al. 2018) we use all available JWST data (both NIRCам and, where available, MIRI). We use the corrected 2nd aperture flux values, corresponding to an aperture of 0.7'' in diameter. In this work, we use a Kroupa (2001) IMF. We note that the simulations use a Chabrier (2003) IMF, but that the difference between the two is minor and less than the errors in obtaining stellar masses and SFRs from photometric SED modelling. We use Planck Collaboration et al. (2020) cosmology throughout.

3. Methods and sample selection

Our selection criteria consists of three steps. Step 1 is an expanded UVJ colour selection via the use of the template fitting code EAZY (Brammer et al. 2008). Step 2 is a specific star-

¹ <https://dawn-cph.github.io/dja/index.html>

formation rate (sSFR) cut after more detailed SED modelling with BAGPIPES (Carnall et al. 2018, 2019b). Finally, step 3 is visual inspection of the SED fits in order to remove poorly fit galaxies or clear contaminants. In addition, for $z > 5$ targets we also implement a brown dwarf removal cut based upon colour-colour selection (Langeroodi & Hjorth 2023; Kokorev et al. 2024a).

3.1. Template fitting with EAZY

We start by using the template fitting code EAZY (Brammer et al. 2008) to compute rest-frame UVJ colours for all the sources within our fields. We use the standard templates included in the DJA analysis pipeline (Valentino et al. 2023). Due to its template fitting approach enabling a wide variety of linear combinations, EAZY allows for a large parameter space of UVJ colours and redshifts. We select galaxies with a photometric redshift above $z = 2$ and with a stellar mass above $M_{\star} = 10^{9.3}$. This then includes sources for which EAZY has underestimated their stellar mass, which could then be recovered by BAGPIPES.

For our initial colour selection, we use two approaches. Our initial attempt used a standard colour selection box (Schreiber et al. 2018). However, it has been shown that there are many quiescent galaxies that fall outside that criterion (Baker et al. 2025b). As we are interested in very high-redshift quiescent galaxies for our fiducial run, we therefore use the updated criteria of Baker et al. (2025b). This corresponds to a UVJ selection criteria of

$$U - V > 1.30 (V - J) - 0.20. \quad (1)$$

This has been shown to fully recover 18 massive high- z spectroscopically confirmed quiescent galaxies and essentially corresponds to a relaxation of the more traditional criteria, including bluer quiescent galaxies. Our primary cut will be based on sSFR which will remove any extra contaminants introduced by this more relaxed approach.

3.2. Spectral energy distribution fitting

To model the spectral energy distribution (SEDs) of our candidate quiescent galaxies we employ the Bayesian SED modelling code BAGPIPES (Carnall et al. 2018, 2019b). See Appendix A for exact details on our setup.

To select quiescent galaxies from those fit we utilise a traditional cut based on sSFR (e.g. Franx et al. 2008; Gallazzi et al. 2014; Schreiber et al. 2018; Carnall et al. 2023a) which corresponds to

$$\text{sSFR} \leq 0.2/t_{\text{age}} \quad (2)$$

where t_{age} is the age of the universe at the observed redshift. In addition, as we are after massive quiescent galaxies, we select those with M_{\star} above $10^{9.5} M_{\odot}$ (except for our analysis of the SMF).

3.3. Visual inspection and Brown Dwarf cut

For candidate $z > 5$ quiescent galaxies with JWST, brown dwarves become interlopers. To deal with this problem we use the selection criteria of Langeroodi & Hjorth (2023) based on brown dwarf templates. This corresponds to a cut of $F200W - F150W > 0.20$. We combine this with a cut from Kokorev et al. (2024a) which was based on selecting for the so called 'Little Red Dots' (LRDs, e.g. Matthee et al. 2024, and many more works). There is still much debate on the nature of LRDs as

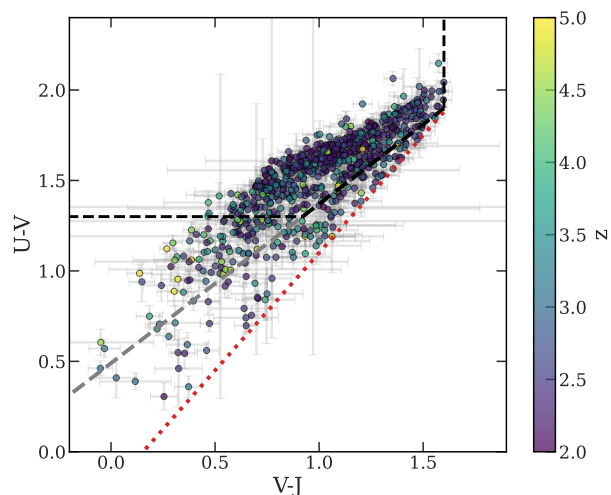


Fig. 1. Upper panel: U-V and V-J colour selection colour-coded by redshift for the massive quiescent galaxies in our full sample. The black line corresponds to the Schreiber et al. (2015) quenching criterion with the grey line addition of the Belli et al. (2019) fast quenching criterion. The red dotted line corresponds to the selection criteria from Baker et al. (2025b) which we use as our initial selection criteria in this work.

to whether they are AGN (e.g. Inayoshi & Maiolino 2025) or quiescent galaxies (e.g. Baggen et al. 2024).² It is likely that they are a combination, making it tricky to remove them from the quiescent galaxies sample. We settle for removing galaxies with clear V shaped SEDs via visual inspection as possible LRD or BD contaminants. Most high- z quiescent galaxies (e.g. those seen in Weibel et al. 2024b; de Graaff et al. 2025; Baker et al. 2025b; Nanayakkara et al. 2025) show blue slopes redwards of the Balmer break so the removal of V shaped SEDs should not affect our selection of these types of massive quiescent galaxies. We also remove candidate quiescent galaxies with insufficient filter coverage to properly probe the Balmer break, as we cannot be certain of those galaxies quiescent nature (this is however, a negligible number of galaxies).³

3.4. Final Sample

Our final sample consists of 745 massive quiescent galaxies with $M_{\star} > 10^{9.5} M_{\odot}$ and with EAZY photometric redshifts of $z > 2$. Fig. 1 shows the distribution of our final sample in UVJ colour space, colour-coded by redshift. We can see that our quiescent galaxy sample primarily occupies the traditional criteria, but with significant numbers within the new Baker et al. (2025b) criteria. These would have been missed by strict UVJ cuts, but have been selected by our new colour selection with confirmation from the sSFR cut. We explore F356W magnitude versus stellar mass binned in redshift for the full sample in Appendix B.

² They may also be both, such as the example of 072127 selected by Kokorev et al. (2024b) as a spectroscopically confirmed broad line AGN LRD and Baker et al. (2025b) as a quiescent galaxy hosting a type-2 AGN.

³ As an example, we remove galaxies with only F200W, F277W, F356W and F444W, if the break is blueward of F200W. We also remove any galaxy with fewer than 4 filters (there are a handful of well-constrained $z = 2$ galaxies with 4 filters that properly probe the full NIR-Cam range). We note that this only applies to the BAGPIPES fitting - we use the full JWST + Hubble filters in the initial EAZY based selection.

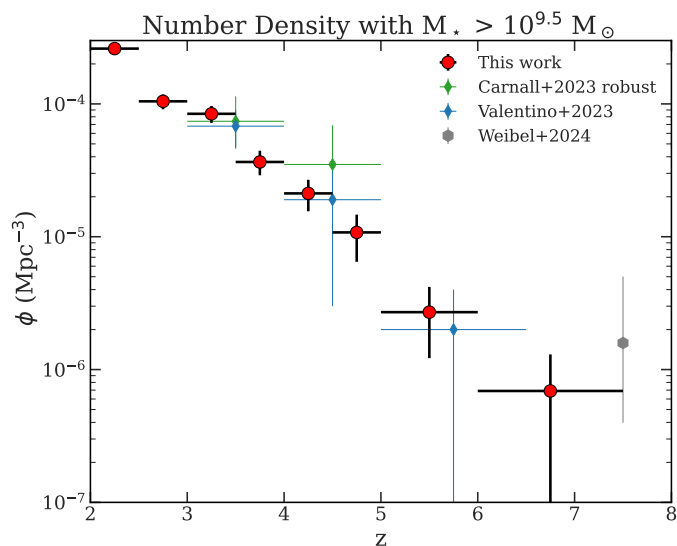


Fig. 2. Quiescent galaxy number densities for those with $M_* > 10^{9.5} M_\odot$ from our sample (red points). We compare to (Carnall et al. 2023a) green points, Valentino et al. (2023) blue points, and the single galaxy from Weibel et al. (2024a) as the grey point.

4. Number densities

The first aspect to explore for the full sample of massive quiescent galaxies is their number densities. In Fig. 2 we show the massive ($M_* > 10^{9.5} M_\odot$) quiescent galaxy number density versus redshift for our study (red markers) and a compilation of other equivalent studies from the literature. The number density is computed as the number of massive quiescent galaxies within a given redshift range divided by the total co-moving volume within that redshift range. The area of each field is computed using the total area of the F444W mosaic for each field, as this is used in computing the detection image in the DJA pipeline (Valentino et al. 2023). The volume is then computed assuming

$$V = \frac{\Omega}{3} \times (d_1^3 - d_2^3). \quad (3)$$

For more details on this method see Baker et al. (2025b) where it is described in detail. As can be seen in Appendix Fig. B.1, even our faintest massive quiescent galaxy is significantly brighter than our shallowest survey limiting magnitude so we do not have to worry about Malmquist bias due to our mass cut of $M_* > 10^{9.5} M_\odot$.

Our errors for the number densities are a combination of three different causes. First we bootstrap the number density calculation for variations in the EAZY redshifts. This enables galaxies to shift redshift bin. This has an almost negligible effect on our number densities. Secondly, we incorporate the effects of cosmic variance. We follow the prescription of Jespersen et al. (2025b), calibrating the cosmic variance based on a combination of the cosmic variance calculator by (Moster et al. 2011) and added constraints from the UniverseMachine simulations (Behroozi et al. 2019) at the highest redshifts. This directly incorporates realistic effects of scatter due to assembly bias (Jespersen et al. 2022; Chuang et al. 2024). This has strong effects on individual fields, but it is less of an issue here due to the combination of separate sightlines and our (comparatively) large area. Thirdly, we include Poisson counting error which becomes the main source of error in the high- z bins. All of these errors are combined in quadrature to produce our overall errors. We follow the same approach when computing errors throughout this work.

The results of this is shown in Fig. 2. We see that we obtain a rapid decline with redshift as would initially be expected. We limit the amount of comparisons here as we wish to (at least) match the exact mass cut used in the literature (see Fig. 3 for many more comparisons to observations and simulations). The most comparable observational study is that of Valentino et al. (2023) as they also select massive quiescent galaxies with $M_* > 10^{9.5} M_\odot$ enabling a more like-for-like comparison, but were limited by the field sizes at that point due to limited publicly available JWST fields. Valentino et al. (2023) had a field size of 145 arcmin², whereas in this work we have an area of 816 arcmin² which is approximately 5× the size. This gives us significantly greater number statistics. They used UVJ selection, but included everything within 1 σ , in effect expanding the criteria.

Our number densities remain mostly consistent with this work despite our much larger field size and redshift range containing $\sim 9\times$ as many quiescent galaxies as in that work. This shows the benefit of selecting multiple different fields in trying to deal with the effects of cosmic variance. We also show the results of Carnall et al. (2023a), which shows an excess in the higher redshift bin due to an overdensity of massive quiescent galaxies in CEERS (Jin et al. 2024; Valentino et al. 2023).

We also compare the number density obtained in Weibel et al. (2024a). This is based on a single $z=7.3$ massive quiescent galaxy obtained as part of the RUBIES survey (de Graaff et al. 2024). A key difficulty in this case is the fact that it is a single galaxy and it is not entirely apparent what volume should be considered for it.⁴ We find a number density slightly lower than was found in Weibel et al. (2024a) but it remains consistent with our $M_* > 10^{9.5} M_\odot$ result.

4.1. Number densities above $M_* > 10^{10} M_\odot$

Due to the number of simulations with limited resolution, and because at lower redshift it is often used as a benchmark, it is also useful to explore the number density of massive quiescent galaxies with $M_* > 10^{10} M_\odot$. This naturally reduces our sample size to around 610 massive quiescent galaxies. We explore their number densities in Fig. 3. We compare them to a selection of other comparable observations and simulations.

Fig. 3 upper panel shows our observed number density versus several comparable studies. Observationally, due to the large volume area probed by our study we are able to use more finely grained binning enabling a greater understanding of the evolution of the number density. Comparing with the literature, there are few JWST era number densities studies with large volumes and most are based on single fields that are likely to be affected by cosmic variance (e.g. Steinhardt et al. 2021; Carnall et al. 2023a; Long et al. 2024; Valentino et al. 2023; Jespersen et al. 2025b). In spite of this, we find good agreement with the results of Baker et al. (2025b), which was based on a small survey area of GOODS-S (also included as a field within this work) but with a correction to the photometric number densities based on their spectroscopic sample. We find significantly more massive quiescent galaxies than those found by Nanayakkara et al. (2025), but this was based on a much smaller area so may be probing an under dense region of massive quiescent galaxies. Again we see the effect of the overdensity in CEERS on the Carnall et al. (2023a) number densities which are significantly higher than ours at $z=4-5$ (but based on only a handful of galaxies in a small area). As shown in the previous section, we again find

⁴ We also note that this galaxy has been recovered as part of our sample in this work.

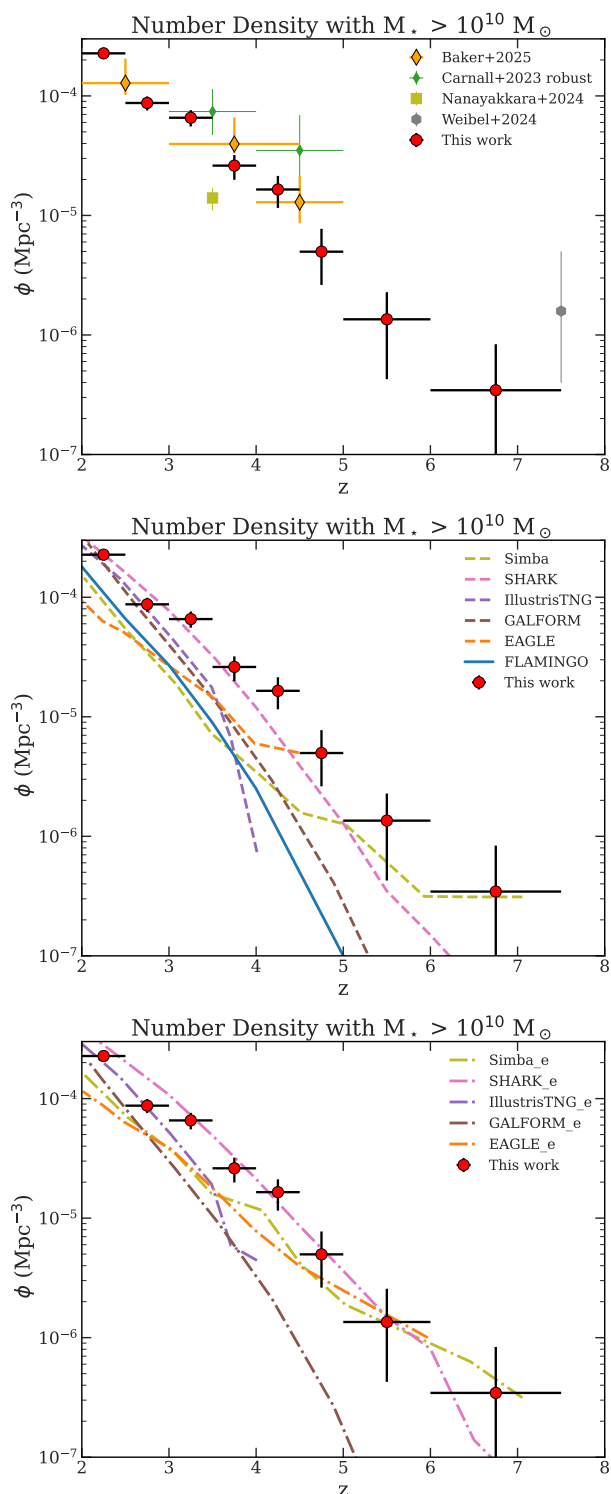


Fig. 3. Quiescent galaxy number densities for $M_* > 10^{10} M_\odot$ from our sample (red points). Upper panel: a comparison to other observational studies, Carnall et al. (2023a) (green points), a spectroscopically corrected sample Baker et al. (2025b) (orange points), a spectroscopically corrected sample Nanayakkara et al. (2025) (light green point) and the Weibel et al. (2024a) point. Middle panel: a comparison to 4 cosmological hydrodynamical simulations EAGLE, ILLUSTRIS-TNG100, SIMBA, and FLAMINGO (Lagos et al. 2025; Baker et al. 2025b) and 2 SAMs (SHARK and GALFORM Lagos et al. 2025). Bottom panel: 3 cosmological hydrodynamical simulations and 2 SAMs, but with Gaussian scatter included in the stellar masses and star-formation rates (e.g. Lagos et al. 2025).

a number density lower than was found in Weibel et al. (2024a) for our $M_* > 10^{10} M_\odot$ number densities.

One of the key benefits of the $M_* > 10^{10} M_\odot$ selection is we can compare more cleanly with simulations and SAMs, as most predictions presented so far in the literature adopt that mass threshold. We first compare to the FLAMINGO simulations (Schaye et al. 2023; Kugel et al. 2023) using the number densities computed in Baker et al. (2025b). These were selected based on the same sSFR criteria adopted here from the 1Gpc^3 simulation box. This enabled them to calculate the effect of cosmic variance on the simulations to up to 3σ . We do not include the errors from that work here as they were computed to match the observed area within that work. However, we do include the observed number density from the simulation as the blue line in the middle panel of Fig. 3. We see that we obtain significantly higher number densities than are found in FLAMINGO at all redshifts probed, which agrees with the findings in Baker et al. (2025b).

The next stage is to compare with other cosmological simulations with different setups, feedback prescriptions, box-sizes, and sub-grid physics. We use the results of Lagos et al. (2025) which consists of 3 cosmological hydrodynamical simulations and 2 SAMs⁵. The cosmological simulations are EAGLE (Schaye et al. 2015; Crain et al. 2015), ILLUSTRIS-TNG100 (Pillepich et al. 2018; Springel et al. 2018), and SIMBA (Davé et al. 2019). The SAMs consist of SHARK (Lagos et al. 2018, 2024) and GALFORM (Lacey et al. 2016). For full details on the simulations see Lagos et al. (2025). Here, we modified the default sSFR selection in Lagos et al. (2025)– based on fixed sSFR thresholds– to match our time-dependent selection of Eq. 2.

The comparison is shown in the middle panel of Fig. 3, where the simulations are denoted by dashed lines. Upper limits from the simulations are not plotted, hence why some tracks end abruptly (these can be envisaged as horizontal lines from the end of each track).

As shown in Lagos et al. (2025), ILLUSTRIS-TNG100 (Pillepich et al. 2018; Springel et al. 2018) shows a significant lack of massive quiescent galaxies above $z=4$ (in fact there are none in the $(100\text{Mpc})^3$ volume, hence it becomes an upper limit), which is thoroughly ruled out by the observations. Note, however, that ILLUSTRIS-TNG100 manages to reproduce the number density of massive quiescent galaxies at $z=2-3$ with $M_* > 10^{10} M_\odot$. A similar result is found for EAGLE, again thoroughly ruled out by our observations. SIMBA also fails to reproduce the observed number densities at almost all redshifts. The same is found for the SAM GALFORM.

On the other hand, the SAM SHARK (Lagos et al. 2018, 2024) appears to agree better with our observed number densities. It remains mostly consistent with our observations up to $z\sim 6$ and only substantially starts to deviate at $z\geq 6$ which is the most unconstrained with simulations. This is likely a result of the AGN feedback prescriptions within SHARK, consisting of a radiative and jet mode feedback (which can be triggered by mergers or disc instabilities, enabling more possible triggers) (Lagos et al. 2025).

The next stage is to try and introduce realistic observational errors in the simulations to attempt to perform a more fair comparison. We follow the approach of Lagos et al. (2025), explained below. Observationally, we have errors on our measured SFRs and stellar masses. These can scatter to both higher or lower values. However, at high- z these will not scatter equally as we have significantly fewer quiescent galaxies than SF galaxies,

⁵ We restrict the analysis here to the simulations used in Lagos et al. (2025) which make their data publicly available

Table 1. Number densities

z	$M_* > 10^{9.5} M_\odot$ ($\times 10^{-5} \text{ Mpc}^{-3}$)	$M_* > 10^{10} M_\odot$ ($\times 10^{-5} \text{ Mpc}^{-3}$)
2.0–2.5	$26.08^{+2.41}_{-2.41}$	$22.70^{+2.16}_{-2.15}$
2.5–3.0	$10.46^{+1.32}_{-1.34}$	$8.73^{+1.17}_{-1.17}$
3.0–3.5	$8.42^{+1.23}_{-1.23}$	$6.57^{+1.03}_{-1.01}$
3.5–4.0	$3.65^{+0.79}_{-0.75}$	$2.61^{+0.59}_{-0.62}$
4.0–5.0	$2.12^{+0.56}_{-0.56}$	$1.65^{+0.49}_{-0.49}$
5.0–6.0	$1.08^{+0.39}_{-0.43}$	$0.50^{+0.28}_{-0.24}$
6.0–7.5	$0.27^{+0.15}_{-0.15}$	$0.14^{+0.09}_{-0.09}$

Notes. Observed number densities for different mass ranges in redshift bins from $z = 2$ to 7.5.

and similarly fewer massive galaxies than lower-mass ones. This means that by including an extra observational error on SFRs and stellar masses from the simulations, we are likely to increase the observed number densities. In the practice, we add gaussian-distributed errors centred on 0 (meaning we assume no bias in our measurements) with a σ of 0.3dex to all stellar masses and SFRs. The sSFR selection criteria is then applied to the resulting quantities. This yields more galaxies making the quiescent cut. The number densities computed from this approach is shown in the lower panel of Fig. 3.

We can see that adding random errors to stellar masses and SFRs changes the number densities from simulations significantly, overall leading to an increase. This increase for the most part is still insufficient for most simulations, which remain below our measurements. In the case of SHARK, adding errors leads to better agreement with the observations.

5. Stellar mass functions

In addition to simply counting the number density of massive quiescent galaxies, we can also explore their mass distribution. To do this, we compute the stellar mass function (SMF) in various bins of redshift. A limitation of previous studies using JWST at these redshifts is their respective survey volume; they have not been large enough to compute a SMF for just the quiescent galaxies. Even with our volume size, we cannot go above $z = 5$, but we can explore the SMF from $z = 2 - 5$. This enables a direct comparison to cosmological simulations and SAMs, albeit with the usual observational caveats.

In our case a key advantage over similar SMF works (e.g. Weaver et al. 2023), is that our entire sample is based upon massive quiescent galaxies. This means that we have more flexibility in our selection and, due to fewer targets, we can use more advanced fitting procedures and visual inspection to remove contaminants. Our selection criteria is necessarily more generous on the colour-side because we know we can trust our sSFR cut followed by visual inspection.

Fig. 4 shows the observed stellar mass function for our sample of high- z massive quiescent galaxies. We compute the stellar mass function for bins of $z = 2 - 2.5$, $z = 2.5 - 3$, $z = 3 - 3.5$, $z = 3.5 - 4$ and finally $z = 4 - 5$. We bin the masses in bins from $10^{9.3} M_\odot < M_* < 10^{11.5} M_\odot$. We reduce the number of mass bins for the highest- z bins due to a lack of very massive galaxies at those redshifts.

We see from Fig. 4 that as z increases we obtain fewer massive quiescent galaxies of all masses (as expected from our number densities results), but also that this is more pronounced for

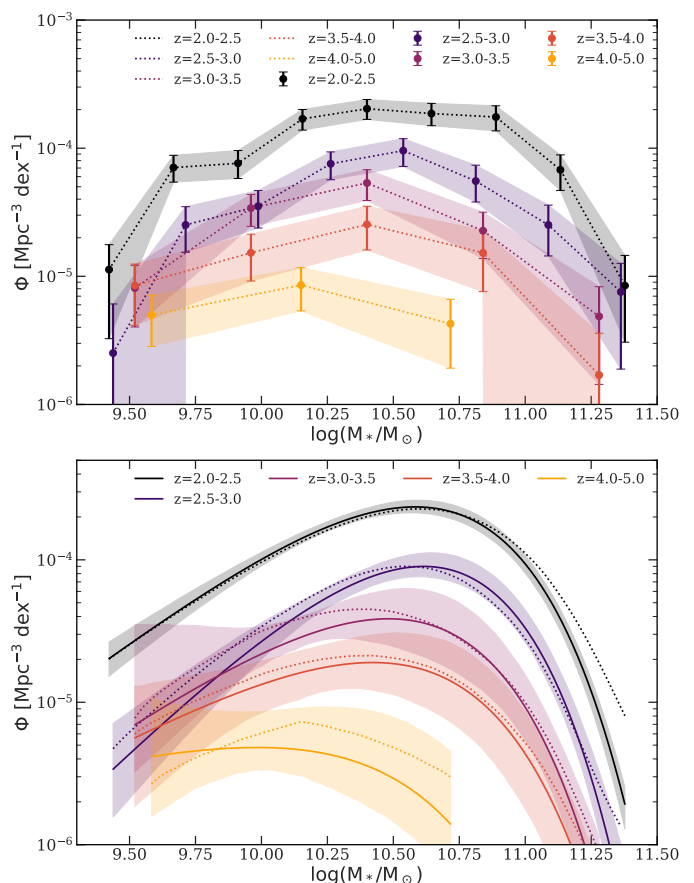


Fig. 4. Upper: observed stellar mass function (Φ) versus stellar mass for massive quiescent galaxies in bins of redshift. Lower: Fitted stellar mass function (Φ) versus stellar mass for massive quiescent galaxies in bins of redshift. The solid line is our best-fit stellar mass functions including the correction for Eddington bias, the dotted lines exclude the Eddington bias correction.

masses closest to the turn over in the SMF. We find that, as has been seen before, there are fewer low-mass and most-massive quiescent galaxies with a decrease towards the lowest and highest mass ends.

In addition, we find a sharp jump in the growth at all masses from $z=4-5$ to $z=3.5-4.0$, mirroring what has been found previously for the overall galaxy population (Weibel et al. 2024b) and for the dust star-forming galaxy population (Gottumukkala et al. 2024). This suggests that during this epoch galaxies could be growing particularly efficiently. We see that the growth in number densities with redshift does appear to have a mass-dependence, with the lower-mass quiescent galaxies experiencing less of an increase with redshift compared to other masses. The next stage is to fit a functional form to the stellar mass function. This will enable a better understanding of its evolution and physics.

5.1. Fitting the SMF

The functional form we will use to fit the stellar mass function is the single Schechter function (Schechter 1976). This function has been shown to well reproduce stellar mass functions of single galaxy populations (e.g. Davidzon et al. 2017; Adams et al.

2021). The Schechter function is defined as follows

$$\Phi(M) dM = \Phi^* \left(\frac{M}{M^*}\right)^\alpha \exp\left(-\frac{M}{M^*}\right) d\left(\frac{M}{M^*}\right) \quad (4)$$

where M^* is the characteristic stellar mass that corresponds to the "knee" of the SMF, the point at which the exponential cut-off and powerlaw slope start. Φ^* is the normalisation and corresponds to the number density at M^* , and α is the strength of the powerlaw slope. Fitting the SMF with a common functional form enables easy comparison between different works and their parameters with more physical meanings.

However, before we fit the functional form, we should explore the relative uncertainties involved in fitting an SMF. This is explored in depth in Appendix C. For now we note that as we are probing massive quiescent galaxies we can detect down to our mass cut. We take into account cosmic variance following the methodology of [Jespersen et al. \(2025b\)](#). Finally, we correct for [Eddington \(1913\)](#) bias via convolving the SMF with a Voigt profile. See Appendix C for full details.

In order to fit the SMF we use the code DYNESTY ([Speagle 2020](#)) which uses Dynamic Nested Sampling ([Skilling 2004](#); [Higson et al. 2019](#)) in order to explore the posterior space for the SMF. This approach better enables degeneracies between various quantities to be explored, whilst also being able to deal with a large number of dimensions within the parameter space. We fit for ϕ^* , M^* and α . We use Uniform priors on all parameters.

The resulting best-fit stellar mass functions are shown in Fig. 4. The errors are obtained from the 16th and 84th percentiles of the resulting distribution of the stellar mass functions computed using the posteriors of the three parameters. This has the effect of propagating through the uncertainties on ϕ^* , M^* and α .

We see that the "knee" of the SMF remains around $10^{10.3-10.5}$ regardless of redshift. This suggests that the switch between high-mass and low-mass quenching mechanisms, typically explained by the knee of the SMF does not appear to vary significantly with redshift.

We see an expected decrease in the normalization of the Schechter function which reiterates our findings with the number densities. We see fewer massive quiescent galaxies of every mass at higher redshift rather than simply seeing a different distribution. However, we do see some tentative evidence for a flattening of the power-law slope α (although this is particularly difficult to constrain). This could suggest that the lower mass quenching mechanism is evolving less with redshift compared to the higher mass mechanism. Alternatively, the greater high-mass build up with redshift may correspond to growth via major or minor mergers ([Puskás et al. 2025](#)), however, recent works have suggested a lack of major mergers among high-*z* massive quiescent galaxies ([Baker et al. 2025b](#); [D'Eugenio et al. 2024](#); [Pascalau et al. 2025](#); [Chittenden et al. 2025](#)). The exact values for the best fit SMFs are reported in Table 2.

5.2. Comparison to simulations

The real power of exploring stellar mass functions for quiescent galaxies comes from comparing them to cosmological simulations and SAM. This is more helpful in our case as we have a larger more robust observational sample, that has been selected primarily based on the same sSFR criteria as from the simulations enabling a more like-to-like comparison. We compare with the compilation explored in [Lagos et al. \(2025\)](#) for $z=3$, and expand this to redshift bins $z=2-2.5$, $z=2.5-3.0$ and $z=4-5$.

We compare with the stellar mass functions from EAGLE, ILLUSTRIS-TNG100, SIMBA, SHARK and GALFORM, in various bins

Table 2. Best-fit stellar mass function parameters

z	M^* $\log(M_\odot)$	ϕ^* $\times 10^{-5} \text{ Mpc}^{-3}$	α
$z=2.0-2.5$	$10.43^{+0.03}_{-0.04}$	$25.79^{+2.14}_{-2.06}$	$1.41^{+0.16}_{-0.14}$
$z=2.5-3.0$	$10.35^{+0.08}_{-0.07}$	$7.98^{+1.48}_{-2.08}$	$1.84^{+0.44}_{-0.39}$
$z=3.0-3.5$	$10.37^{+0.28}_{-0.12}$	$4.37^{+1.53}_{-2.20}$	$1.29^{+0.70}_{-1.16}$
$z=3.5-4.0$	$10.42^{+0.15}_{-0.16}$	$2.24^{+0.98}_{-1.16}$	$1.01^{+0.85}_{-0.62}$
$z=4.0-5.0$	$10.33^{+0.98}_{-0.28}$	$0.47^{+0.57}_{-0.40}$	$0.46^{+1.31}_{-1.00}$

Notes. The best-fit [Schechter \(1976\)](#) function parameters for each SMF fit for each redshift

from $z = 2 - 5$. In order to match the observed bins of our observation we average over the available simulation snapshots' SMF within that bin. The results are shown in the left panel of Fig. 5. Our observed SMF is given by the solid lines and shaded region, whilst the results from the simulations is given by the dashed line. We can see immediately that none of the cosmological simulations or SAMs fully reproduce the observed SMF for the massive quiescent galaxies at any redshift probed in this work. As was found by [Lagos et al. \(2025\)](#) for $z=3$, some simulations and SAMs over produce lower mass quiescent galaxies and under produce higher mass, whilst others fail to reproduce enough high-mass galaxies.

There is a large disagreement between the simulations themselves on the shapes of the quiescent galaxy SMFs as well, largely a product of the different feedback implementations ([Lagos et al. 2025](#)). This shows that even SAMs such as SHARK, which accurately reproduce the observed number densities for $M_\star > 10^{10} M_\odot$, cannot reproduce the observed mass distribution.

In the right-hand panel of Fig. 5 we compare to the simulations with the addition of the gaussian errors on the observed quantities (stellar mass and SFR). These are denoted with the dot-dash lines. Adding errors has the effect of broadening the SMF, particularly helping to reproduce the higher-mass end, in the cases where the models struggle with producing enough high-mass galaxies, but there are still significant differences with the observations. This is again most apparent at the lower mass end, with EAGLE being the closest to reproducing the SMF there, but largely failing at the high mass end.

5.3. Field-to-field and colour selection variations

Due to our use of several different fields in different regions of the sky, we can investigate possible field-to-field variations in the SMF. We only compute this from redshift 2–2.5, 2.5–3, and 3–3.5 in order to ensure we have enough galaxies for our bins. The results of this are shown in Fig. 6. The upper panel shows the SMF computed on individual fields, in this case PRIMER-UDS, PRIMER-COSMOS, CEERS-EGS, and GOODS. Also overplotted is the equivalent SMF from [Weaver et al. \(2023\)](#).

We can immediately see that there is a natural variation in the stellar mass functions for each field, particularly at the low-mass end. CEERS clearly has the greatest number of quiescent galaxies for its area at the low-mass end, which mirrors previous results finding an overabundance of massive quiescent galaxies within this field ([Jin et al. 2024](#); [Ito et al. 2025](#); [Valentino et al. 2023](#)). Meanwhile, GOODS-S varies significantly depending on masses. This is showing that cosmic variance does have an effect, particularly on small survey areas, and that one should take into account multiple different fields with different positions on the

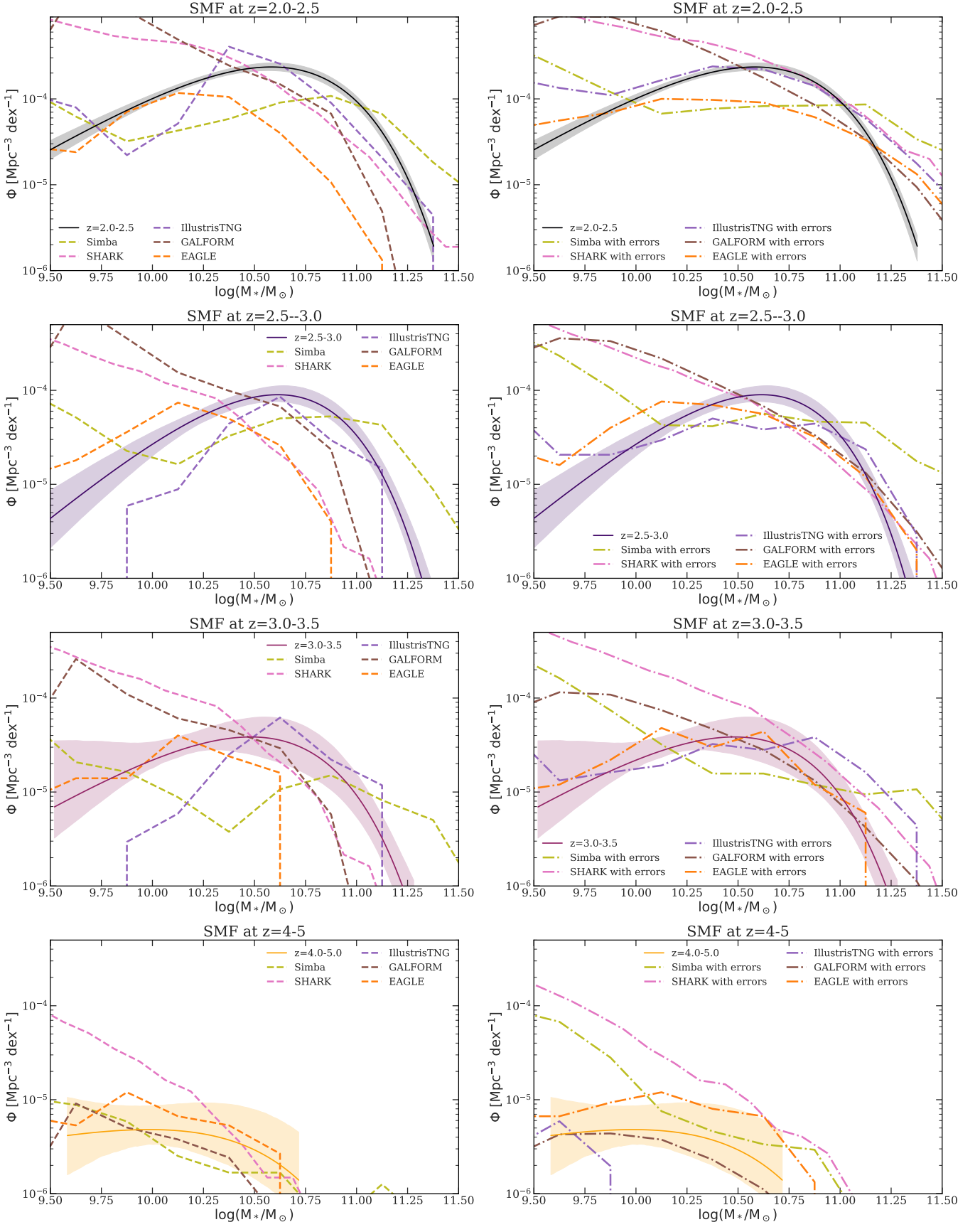


Fig. 5. Comparison between our observed stellar mass function (solid lines) at $z = 2-2.5$ (upper panel) $z = 2.5-3$ (upper middle panel), $z = 3-3.5$ (lower middle panel) and $z = 4-5$ (lower panel), alongside 5 cosmological simulations denoted by dashed lines (left hand panels) (Lagos et al. 2025). The right hand panel shows the same but with Gaussian scatter added to the stellar masses and SFRs for the 5 simulations (e.g. Lagos et al. 2025).

Quiescent Galaxy SMFs for Individual Fields

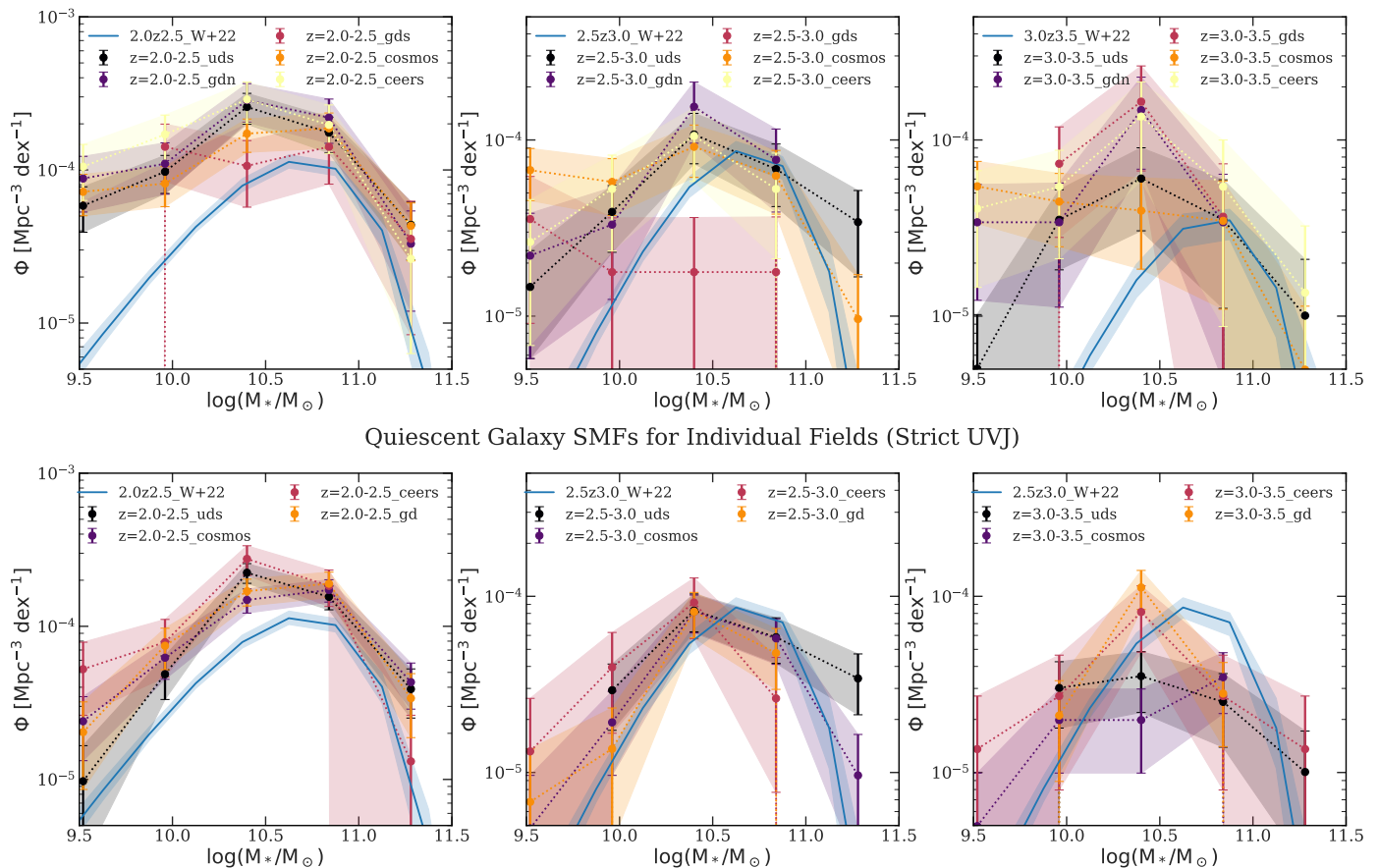


Fig. 6. Upper panels: field-to-field variations in the SMF with the same selection criteria as previously. We also plot the fitted SMF from [Weaver et al. \(2023\)](#) in blue for their quiescent galaxy sample. Left for $z = 2 - 2.5$, middle for $z = 2.5 - 3.0$ and right for $z = 3.0 - 3.5$. We see significant field-to-field variations underlining the effects of cosmic variance in small field observations. This increases at higher redshifts. Lower panels: the same but using a stricter UVJ cut to better replicate the selection criteria of [Weaver et al. \(2023\)](#). We find greater consistency with the [Weaver et al. \(2023\)](#) results, highlighting the importance of selection criteria in obtaining as many quiescent galaxies as possible.

sky when computing number densities and SMFs for massive quiescent galaxies.

For the $z=2.5-3$ bin we see much more variation, showing the increasing impact of cosmic variance at higher- z when sources become rarer. This becomes even more pronounced at $z=3-3.5$, where we can see clear differences between the shapes and values of the SMFs between the various fields. It should also be noted that we are probing the redshift ranges least affected in our study here (as we cannot probe this effect at much higher z because of a lack of galaxies). Therefore, this provides strong evidence that cosmic variance will play a role for individual fields, as we clearly see this effect at $z = 2.5-3.5$. We also see that for the $z=2-2.5$ bin in particular, we see many more lower mass massive quiescent galaxies than were found in [Weaver et al. \(2023\)](#). We now explore what is driving this offset.

In the lower panel of Fig. 6 we show SMFs computed with a much stricter UVJ selection. We use the [Schreiber et al. \(2015\)](#) criteria. Whilst not the same selection criteria as [Weaver et al. \(2023\)](#), it is more strict than our sSFR criteria and should enable any variation to be seen. There is a clear drop in the number of low-mass massive quiescent galaxies seen at $z=2-2.5$, $z=2.5-3$ and $z=3-3.5$. We become much more consistent with the results of [Weaver et al. \(2023\)](#). This once again highlights the importance of a broad selection criteria (i.e. Bayesian based SED modelling in addition to colours) in order to accurately uncover

massive quiescent galaxies and suggests that the [Weaver et al. \(2023\)](#) (and many other studies), are missing significant numbers of lower mass quiescent galaxies through their selections.

5.4. Stellar mass density of massive quiescent galaxies

Another area of interest is exploring the stellar mass density (SMD) of a particular population of galaxies in the universe (e.g. [Madau & Dickinson 2014](#)). This can be computed a number of ways (e.g. from the cosmic star-formation rate density) but in our case this a straightforward matter of integrating the obtained stellar mass functions at each redshift. We use our fitted form of the stellar mass function with a commonly chosen lower mass limit of $M_* > 10^8 M_\odot$.⁶ We integrate using our best fit Schechter function for each redshift, extrapolating to lower masses than those explored in our SMFs.

Fig. 7 shows our stellar mass density versus redshift compared to other studies. It shows that we are seeing a steeper evolution in our SMD compared to other studies such as [Weaver et al. \(2023\)](#). We find less mass per unit volume at higher redshifts but more mass at lower z .⁷ The increase in ρ_* at $z=2-2.5$ is

⁶ We test varying this as the simulations only go down to $10^9 M_\odot$ and find it makes no appreciable difference, as the very low-mass end is sub-dominant.

⁷ We note that we fully propagate through the errors from our SMF.

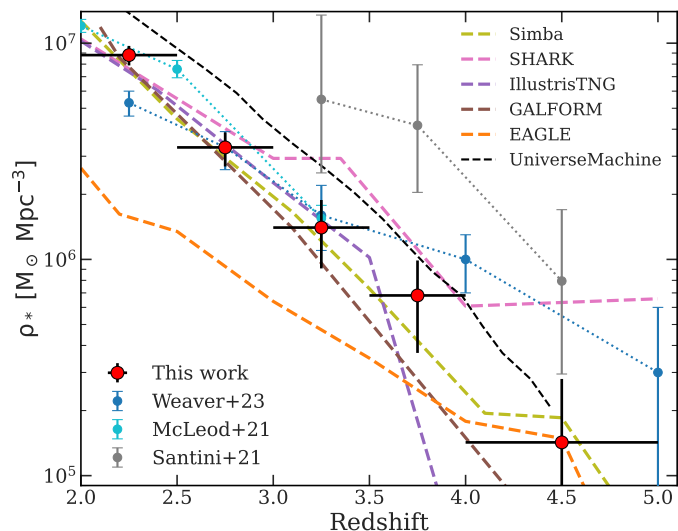


Fig. 7. Stellar mass density of quiescent galaxies versus redshift based upon our best-fit SMFs (red points). Overplotted is a comparison for quiescent galaxies from Weaver et al. (2023) (blue points), Santini et al. (2021) (grey points), McLeod et al. (2021) (light blue points) and theoretical predictions from UNIVERSEMACHINE (Behroozi et al. 2019) (black dashed line). We also overplot results from SIMBA, SHARK, ILLUSTRIS-TNG100, GALFORM, and EAGLE by integrating their SMFs.

in keeping with our findings for the number densities and SMFs where we see an overabundance compared to other works. Interestingly, this is not the case at $z=2.5-3$ or $z=3-3.5$ which match the results of Weaver et al. (2023) (as can be seen in Fig. 5). We find that the SMD increases by a factor of $\times 5$ from $z = 4.5$ to $z=3.75$, then increases by around a factor of $\times 2$ between each lower redshift bin.

We also compare our results to two pre-JWST works, Santini et al. (2021) and McLeod et al. (2021). We find reasonable agreement with McLeod et al. (2021), particularly at $z=3-3.5$, but find significantly lower mass per unit volume than Santini et al. (2021). We also again compare with cosmological simulations and SAMs. We find EAGLE dramatically fails to reproduce the observed SMD. ILLUSTRIS-TNG100 produces it up to $z=3.5$ where it dramatically falls (due to having no high- z massive quiescent galaxies). SHARK overpredicts the SMD at $z>3.0$. GALFORM slightly underpredicts it at $z>3$.

Interestingly, SIMBA well reproduces the SMD. This is surprising as it failed to reproduce the observed number densities or SMF, but goes to show how difficult it is to accurately reproduce all of these within the same simulation. Clearly the shape of the SMFs in SIMBA is dramatically different to observations, but the area underneath remains the same. We also overplot predictions from UNIVERSEMACHINE (Behroozi et al. 2019; Weaver et al. 2023) which slightly over predicts the SMD at each redshift, i.e. the normalisation is too high, but it matches the shape well.

The increase in the stellar mass density with redshift appears larger in our work (i.e. $5\times$ larger from $z=4.5$ to $z=3.75$) than many previous works (i.e. the slope is steeper). This suggests that we are seeing more massive quiescent galaxy assembly from $z = 5$ to $z = 2$ than previously seen which corresponds to an increase in stellar mass per unit volume of about 60 times between $z=4.5$ and $z=2$. This is in-keeping with an increase in quenching activity.

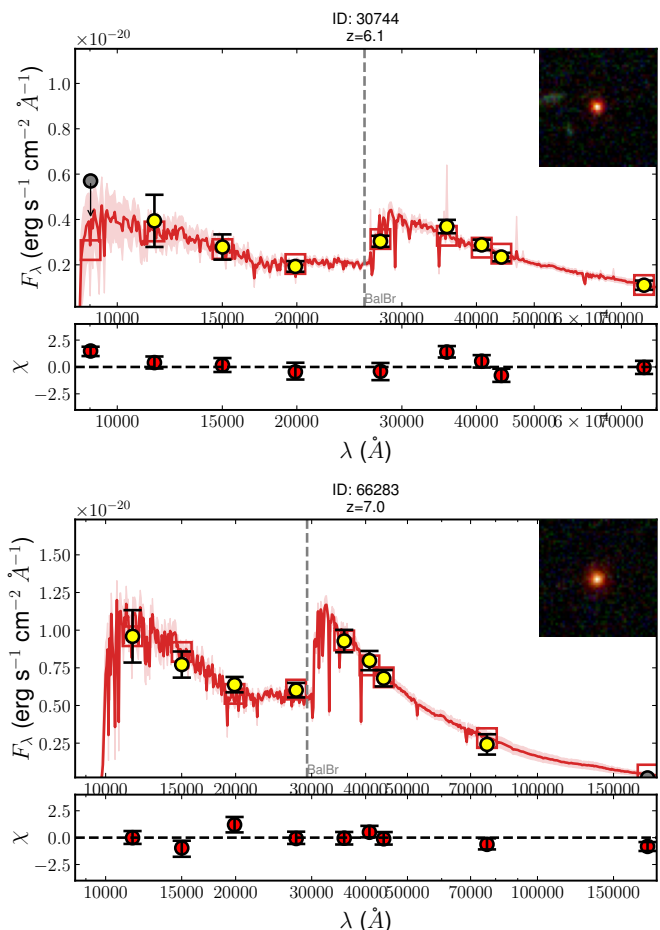


Fig. 8. SED fits for our two highest redshift candidates (the highest- z of which is confirmed by spectroscopy Weibel et al. 2024a). The yellow points are the observed photometry and the grey points correspond to non-detections with a $\text{SNR}<3$. The red-squares correspond to the best-fit model photometry and the red line corresponds to the best-fit model spectrum. Uncertainties in the best-fit model spectrum are denoted by the shaded regions which correspond to the 16th and 84th percentiles of the resulting distribution. An RGB image of the galaxy is in the upper right of the figure. Both galaxies have MIRI coverage constraining the NIR part of the SED.

6. High- z candidates

Finally, we explore the high-redshift end of our massive quiescent galaxy sample. Fig. 8 shows SEDs and RGB images of our two $z>6$ quiescent galaxies as identified by our selection criteria. For more details on our selection criteria for the highest redshift candidates, see Appendix D.

The first key aspect is the recovery of 66283 which has previously been identified and published in Weibel et al. (2024a) and is a spectroscopically confirmed quiescent galaxy that lies at $z=7.3$. We note that our best fit EAZY photometric redshift is out by around 0.3, but that this is due to the difficulty of constraining a precise redshift from the Balmer break alone. Due to our wide redshift ranged bins for the highest- z massive quiescent galaxies, this is not going to significantly affect our results. Our other $z>6$ target is 30744 at $z=6.1$ which shows clear Balmer break in the photometry and has the benefit of a MIRI detection at $770\mu\text{m}$. This makes it a robust candidate that would be worth following up in the future with spectroscopy.

7. Discussion

7.1. Observations

In this work we have explored a large sample of massive quiescent galaxies from $z=2-7$, investigating their number densities, stellar mass functions and stellar mass density. Previous JWST studies have reported significantly larger number densities compared to previous works and simulations (e.g. Carnall et al. 2023a; Valentino et al. 2023; Albers et al. 2024; Long et al. 2024; Baker et al. 2025b). It is complicated to compare like with like due to the number of differences between selection and how these affect the number density values. As has been shown previously, and comprehensively in this work, selections based on colours and sSFR give different results, especially at high- z . In addition to this, the actual mass cut for selecting massive quiescent galaxies varies between works with some studies using $M_{\star} > 10.6$ and others $M_{\star} > 10$. In this work, we have tried to homogenise as much as possible by providing two different cuts, a $M_{\star} > 10^{9.5} M_{\odot}$ cut and an $M_{\star} > 10^{10} M_{\odot}$ cut (the latter providing more literature comparisons).

Regarding the number densities, we find strong agreement with previous works such as Valentino et al. (2023) and Baker et al. (2025b). This is likely due to the expanded quiescent galaxy selection criteria within these works. We find a greater number of massive quiescent galaxies than Nanayakkara et al. (2025), but fewer than Carnall et al. (2023a) found in the CEERS overdensity. At the high- z end, we find roughly the same number as that reported in Weibel et al. (2024a), but again caution that their reported value is based on a single source).

What we are learning from this is the importance in both probing large volumes to combat cosmic variance, but also that we need a combination of different fields which are better able to sample the underlying large-scale structure, making the number densities more robust to the effects of over- or under-densities (Valentino et al. 2023; Jespersen et al. 2025b).

This is seen again in the SMFs. We test the effects of cosmic variance and colour selection on our results, finding field-to-field variations (again reiterating the result of Valentino et al. 2023, but this time for the high- z quiescent galaxy SMFs) that become increasingly pronounced at higher z . We also find significant differences based on our selection criteria, showing how just using colour selection can lead to significantly reduced SMFs on the low-mass end (compared to an expanded colour selection followed by detailed SED modelling).

The "knee" of the fitted SMFs remains within $10^{10.3-10.5}$ regardless of redshift, suggesting that the quenching processes are operating consistently at the same mass ranges, i.e. the turnover between quenching regimes is redshift independent. We see tentative signs of upturns at the low-mass end for our observed SMFs, particularly in the individual fields. Whilst we caution that we may be affected by bin edge effects and low-number statistics, this is possibly a sign of environmental effects playing a role in quenching. Indeed, more local galaxies with stellar masses $10^9 - 10^{10} M_{\odot}$ would be prime targets for environmental quenching (Peng et al. 2010; Hamadouche et al. 2024). This would also explain why we see more field-to-field variation in the lower-mass end of the SMFs – this is simply due to the varying sizes and environments of the individual fields.

This further motivates combining multiple wide-area JWST surveys with many different filters that probe various fields to better sample the underlying large-scale structure. In addition, shallower, wide field surveys such as COSMOS-Web (Casey et al. 2023) will be important in understanding variations within particular fields (albeit with a reduction in available bands and

depth). In addition to JWST, instruments such as EUCLID (Euclid Collaboration et al. 2025; Weaver et al. 2025), while significantly more shallow and with fewer bands, will also be vital in studying the effects of cosmic variance on the high- z SMF.

We integrate our SMFs in order to compute the cosmic SMD of massive quiescent galaxies and compare to other observational results (Santini et al. 2021; McLeod et al. 2021; Weaver et al. 2023). We find a sharper rise in the mass density from $z=4$ to 2 than has been seen previously (Weaver et al. 2023), highlighting that we see a sharp rise in the amount of mass locked up in these quiescent systems in the period up towards cosmic noon, increasing by a factor of $\times 60$ from $z=4.5$ to $z=2$. This may be down to the increasing importance of quenching these massive quiescent galaxies compared to what was previously found.

In accurately determining quiescent galaxies from photometry, increased band coverage is crucial for helping remove interlopers such as Brown Dwarves and LRDs at the highest redshifts (e.g. above $z = 5$). Dedicated medium bands surveys among pre-existing fields are incredibly useful for this (e.g. Williams et al. 2023; Eisenstein et al. 2023a; Suess et al. 2024). Greater understanding of the interloper populations will also be vital to better understand and remove them. We report one strong $z > 6$ quiescent galaxy candidate with the addition of a MIRI detection.

7.2. Simulations

Regarding simulations, predictions differ wildly between them. With a mass cut of $M_{\star} > 10^{10} M_{\odot}$ we find poor agreement with most cosmological hydrodynamical simulations and SAMs. FLAMINGO (Schaye et al. 2023) and ILLUSTRIS-TNG100 (Pillepich et al. 2018; Springel et al. 2018) perform most poorly, with neither of these works having close to enough massive quiescent galaxies, failing to reproduce the observed number densities above $z=3$. ILLUSTRIS-TNG100 does however manage to reproduce the observed number densities at $z = 2 - 3$. Interestingly, FLAMINGO, SIMBA (Davé et al. 2019), and EAGLE (Schaye et al. 2015; Crain et al. 2015) all fail to produce the number densities at $z=2-3$, despite this range being the most well-constrained by observations. GALFORM (Lacey et al. 2016) and ILLUSTRIS-TNG100 struggle at higher- z , i.e. above $z=3.5$. SHARK (Lagos et al. 2018, 2024) performs better, generally matching the number densities up to $z=4$, but sees deviations at higher redshifts.

We also explored including errors in the simulations to better mimic observations, finding that while this changes the number densities, it cannot account for the discrepancies seen (although this pushes SHARK to reasonably accurately predict the number density). This highlights the difficulty in obtaining accurate number densities at all redshifts with simulations.

A more in-depth question is whether they can produce the observed mass distribution of these massive quiescent galaxies and this is tested by the stellar mass function. We find that none of the simulations appears to reproduce the quiescent galaxy stellar mass function as observed in this work (or in Weaver et al. (2023)) at any redshift (although ILLUSTRIS-TNG100 is close at $z = 2 - 5$). Predictions are again disparate with some simulations obtaining enough high-mass quiescent galaxies, but failing at the low-mass end, whilst others can reproduce the low-mass, but fail at the high-mass end. These discrepancies still hold after adding gaussian-distributed errors on simulated quantities. This has the effect of broadening the simulated SMFs.

We also see that several simulations fail to fully-reproduce the SMD of quiescent galaxies across cosmic time, but interestingly most remain within 2σ of the observations (with the exception of EAGLE), and the dramatic differences seen in the SMF

are mostly washed out, with most simulations producing SMDs within 0.3 dex of each other. EAGLE dramatically under-predicts, whilst ILLUSTRIS-TNG100 fails at $z > 3.5$ (due to a lack of quiescent galaxies). Despite obtaining the closest number densities, SHARK overpredicts the SMD at $z > 3$ due to its significantly larger population of lower mass quiescent galaxies. SIMBA and GALFORM appear mostly able to reproduce the observed SMD (despite struggling with the number densities and SMFs).

As has previously been reported in Lagos et al. (2025) for $z = 3$, these findings for the simulations are likely due to the varying feedback prescriptions with them, in particular when AGN feedback kicks in and the relative strength of it. Simulations where it only kicks in after a certain mass range (e.g. ILLUSTRIS-TNG100) struggle to reproduce any of the less massive quiescent galaxies. Meanwhile, other simulations such as EAGLE well reproduce the low-mass end of the SMFs but cannot produce high-mass quiescent galaxies, showing that their high-mass quenching mechanisms need stronger or more efficient feedback. We see from the SMFs that the lower mass quenching mechanisms appear to be much too strong within the SAMs SHARK and GALFORM. SIMBA fails to reproduce the shape of the SMF at either low or high-mass ends, suggesting both require adjustments.

Resolution effects and box-sizes are also important. As has been shown previously in Baker et al. (2025b), simulation based number densities are also subject to cosmic variance because of their inherent small box sizes. Whilst large volume simulations exist (e.g. FLAMINGO) they often struggle to match the required small-scale physics to produce enough massive quiescent galaxies (as seen for FLAMINGO in Baker et al. 2025b). This suggests that large-volume simulations are crucial to try and minimise the effects of cosmic variance even within the simulations, but that they also need more complicated feedback prescriptions in order to reproduce observations.

On the other hand, quenching both massive and low-mass galaxies is a multi scale problem (Man & Belli 2018; De Lucia et al. 2025) with many of the crucial feedback processes taking place at much smaller scales. This motivates further research into the quenching mechanisms within these highly resolved simulations. However, this proves to be a big challenge for simulations as they can either aim for a large box (sacrificing resolution and resorting to sub-grid physics) or they can resolve the small scale physics but only for a handful of galaxies which is too small for number densities or SMFs (for a review of the problem see Vogelsberger et al. 2020). Small-scale simulations also struggle to find massive quiescent galaxies at high z due to their relative rarity within the overall galaxy population.

Overall, future wide and deep JWST surveys (combined with legacy data) and the next generation of cosmological hydrodynamical simulations and SAMs will start to address these issues.

8. Conclusions

We have put together a robust sample of over 700 massive quiescent galaxies from $z = 2 - 7$ from a combination of some of the deepest JWST multi-band surveys with an overall area $5\times$ larger than existing JWST studies. We computed quiescent galaxy number densities at redshifts $z = 2 - 7$ and explored stellar mass functions and the stellar mass density from $z = 2 - 5$. We compare to a range of simulations and SAMs with matching selection criteria to provide an accurate comparison to the state-of-the-art galaxy evolutionary modelling. Our key findings are as follows.

1. We confirm an overabundance of massive quiescent galaxies relative to pre-JWST works and models at high- z .
2. We find significant numbers of observed massive quiescent galaxies that would be missed by the traditional UVJ colour selection criteria, further motivating cuts based on sSFR.
3. We find no cosmological simulations that we explore can accurately predict the observed number density of massive quiescent galaxies.
4. Simulations cannot reproduce the observed quiescent galaxy SMF at any redshift from $z = 2 - 5$. All fail to match the shape and normalisation of the observed SMF. Some models overpredict lower-mass quiescent galaxies (e.g. SHARK, GALFORM) and fail at the high-mass end, whilst others such as ILLUSTRIS-TNG100 match the high-mass end but fail to quench any lower-mass galaxies. This is linked to the various feedback prescriptions in the simulations.
5. Quiescent galaxy stellar mass functions can vary significantly with differing selection criteria, and we uncover more quiescent galaxies at the lower mass end than previous studies. This is due to our extended colour selection and our sSFR cut being better able to uncover the lower-mass quiescent galaxy population.
6. We show the impact of field-to-field variation in SMFs due to cosmic variance and show how it significantly increases at higher redshift. We also show significant variations when different colour selection criteria are used compared to a sSFR cut.
7. We find that the stellar mass density of quiescent galaxies evolves more steeply between $z = 5$ and $z = 2$ than has been found in previous work, indicating a significant increase in the importance of galaxy quenching within these epochs.
8. As part of the sample, we report another strong high- z ($z > 6$) quiescent galaxy candidate.

Acknowledgements. WMB would like to acknowledge support from DARK via the DARK Fellowship. This work was supported by a research grant (VIL54489) from VILLUM FONDEN. WMB would like to thank Francesco D'Eugenio and Marko Shuntov for helpful and enlightening discussions. We acknowledge use of ASTROPY (Astropy Collaboration et al. 2013), FPS (Conroy et al. 2009; Conroy & Gunn 2010), EAZY (Brammer et al. 2008), GRIZLI (Brammer 2023), BAGPIPES (Carnall et al. 2018, 2019b), NUMPY (Harris et al. 2020), DYNESTY (Speagle 2020), MATPLOTLIB (Hunter 2007), and TOPCAT (Taylor 2005).

References

- Adams, N. J., Bowler, R. A. A., Jarvis, M. J., Häußler, B., & Lagos, C. D. P. 2021, MNRAS, 506, 4933
- Alberts, S., Williams, C. C., Helton, J. M., et al. 2024, ApJ, 975, 85
- Antwi-Danso, J., Papovich, C., Esdaile, J., et al. 2025, ApJ, 978, 90
- Antwi-Danso, J., Papovich, C., Leja, J., et al. 2023, ApJ, 943, 166
- Astropy Collaboration, Robitaille, T. P., Tollerud, E. J., et al. 2013, A&A, 558, A33
- Baggen, J. F. W., van Dokkum, P., Brammer, G., et al. 2024, ApJ, 977, L13
- Baker, W. M., D'Eugenio, F., Maiolino, R., et al. 2025a, A&A, 697, A90
- Baker, W. M., Lim, S., D'Eugenio, F., et al. 2025b, MNRAS, 539, 557
- Baker, W. M., Maiolino, R., Bluck, A. F. L., et al. 2024, MNRAS, 534, 30
- Barrufet, L., Oesch, P. A., Marques-Chaves, R., et al. 2025, MNRAS, 537, 3453
- Beckmann, R. S., Devriendt, J., Slyz, A., et al. 2017, MNRAS, 472, 949
- Behroozi, P., Wechsler, R. H., Hearin, A. P., & Conroy, C. 2019, MNRAS, 488, 3143
- Belli, S., Newman, A. B., & Ellis, R. S. 2019, ApJ, 874, 17
- Brammer, G. 2023, grizli
- Brammer, G. B., van Dokkum, P. G., & Coppi, P. 2008, ApJ, 686, 1503
- Bressan, A., Marigo, P., Girardi, L., et al. 2012, MNRAS, 427, 127
- Bruzual, G. & Charlot, S. 2003, MNRAS, 344, 1000
- Byler, N., Dalcanton, J. J., Conroy, C., & Johnson, B. D. 2017, ApJ, 840, 44
- Calzetti, D., Armus, L., Bohlin, R. C., et al. 2000, ApJ, 533, 682
- Carnall, A. C., Cullen, F., McLure, R. J., et al. 2024, MNRAS, 534, 325
- Carnall, A. C., Leja, J., Johnson, B. D., et al. 2019a, ApJ, 873, 44
- Carnall, A. C., McLeod, D. J., McLure, R. J., et al. 2023a, MNRAS, 520, 3974

- Carnall, A. C., McLure, R. J., Dunlop, J. S., et al. 2019b, *MNRAS*, 490, 417
- Carnall, A. C., McLure, R. J., Dunlop, J. S., & Davé, R. 2018, *MNRAS*, 480, 4379
- Carnall, A. C., McLure, R. J., Dunlop, J. S., et al. 2023b, *Nature*, 619, 716
- Casey, C. M., Kartaltepe, J. S., Drakos, N. E., et al. 2023, *ApJ*, 954, 31
- Chabrier, G. 2003, *PASP*, 115, 763
- Chevallard, J. & Charlot, S. 2016, *MNRAS*, 462, 1415
- Chittenden, H. G., Glazebrook, K., Nanayakkara, T., et al. 2025, arXiv e-prints, arXiv:2504.19696
- Chuang, C.-Y., Jespersen, C. K., Lin, Y.-T., Ho, S., & Genel, S. 2024, *ApJ*, 965, 101
- Conroy, C. 2013, *ARA&A*, 51, 393
- Conroy, C. & Gunn, J. E. 2010, *ApJ*, 712, 833
- Conroy, C., Gunn, J. E., & White, M. 2009, *ApJ*, 699, 486
- Crain, R. A., Schaye, J., Bower, R. G., et al. 2015, *MNRAS*, 450, 1937
- Croton, D. J., Springel, V., White, S. D. M., et al. 2006, *MNRAS*, 365, 11
- Curtis-Lake, E., Bluck, A., d'Eugenio, F., Maiolino, R., & Sijacki, D. 2023, *Nature Astronomy*, 7, 247
- Davé, R., Anglés-Alcázar, D., Narayanan, D., et al. 2019, *MNRAS*, 486, 2827
- Davidzon, I., Ilbert, O., Laigle, C., et al. 2017, *A&A*, 605, A70
- de Graaff, A., Brammer, G., Weibel, A., et al. 2024, arXiv e-prints, arXiv:2409.05948
- de Graaff, A., Setton, D. J., Brammer, G., et al. 2025, *Nature Astronomy*, 9, 280
- De Lucia, G., Fontanot, F., Hirschmann, M., & Xie, L. 2025, arXiv e-prints, arXiv:2502.01724
- De Lucia, G., Fontanot, F., Xie, L., & Hirschmann, M. 2024, *A&A*, 687, A68
- Dekel, A. & Silk, J. 1986, *ApJ*, 303, 39
- D'Eugenio, F., Pérez-González, P. G., Maiolino, R., et al. 2024, *Nature Astronomy*, 8, 1443
- Dome, T., Tacchella, S., Fialkov, A., et al. 2024, *MNRAS*, 527, 2139
- Donnan, C. T., McLure, R. J., Dunlop, J. S., et al. 2024, *MNRAS*, 533, 3222
- Donnari, M., Pillepich, A., Joshi, G. D., et al. 2021a, *MNRAS*, 500, 4004
- Donnari, M., Pillepich, A., Nelson, D., et al. 2021b, *MNRAS*, 506, 4760
- Dressler, A. 1980, *ApJ*, 236, 351
- Dunlop, J. S., Abraham, R. G., Ashby, M. L. N., et al. 2021, PRIMER: Public Release IMaging for Extragalactic Research, JWST Proposal. Cycle 1, ID. #1837
- Eddington, A. S. 1913, *MNRAS*, 73, 359
- Eisenstein, D. J., Johnson, B. D., Robertson, B., et al. 2023a, arXiv e-prints, arXiv:2310.12340
- Eisenstein, D. J., Willott, C., Alberts, S., et al. 2023b, arXiv e-prints, arXiv:2306.02465
- Euclid Collaboration, Mellier, Y., Abdurro'uf, et al. 2025, *A&A*, 697, A1
- Fabian, A. C. 2012, *ARA&A*, 50, 455
- Falcón-Barroso, J., Sánchez-Blázquez, P., Vazdekis, A., et al. 2011, *A&A*, 532, A95
- Finkelstein, S. L., Bagley, M. B., Arrabal Haro, P., et al. 2025, *ApJ*, 983, L4
- Franx, M., van Dokkum, P. G., Förster Schreiber, N. M., et al. 2008, *ApJ*, 688, 770
- Gallazzi, A., Bell, E. F., Zibetti, S., Brinchmann, J., & Kelson, D. D. 2014, *ApJ*, 788, 72
- Gelli, V., Pallottini, A., Salvadori, S., et al. 2025, arXiv e-prints, arXiv:2501.16418
- Giavalisco, M., Ferguson, H. C., Koekemoer, A. M., et al. 2004, *ApJ*, 600, L93
- Gottmukkala, R., Barrufet, L., Oesch, P. A., et al. 2024, *MNRAS*, 530, 966
- Grazian, A., Fontana, A., Santini, P., et al. 2015, *A&A*, 575, A96
- Grogin, N. A., Kocevski, D. D., Faber, S. M., et al. 2011, *ApJS*, 197, 35
- Gunn, J. E. & Gott, III, J. R. 1972, *ApJ*, 176, 1
- Hamadouche, M. L., McLure, R. J., Carnall, A., et al. 2024, arXiv e-prints, arXiv:2412.09592
- Harris, C. R., Millman, K. J., van der Walt, S. J., et al. 2020, *Nature*, 585, 357
- Heintz, K. E., Brammer, G. B., Watson, D., et al. 2025, *A&A*, 693, A60
- Higson, E., Handley, W., Hobson, M., & Lasenby, A. 2019, *Statistics and Computing*, 29, 891
- Hunter, J. D. 2007, *Computing in Science & Engineering*, 9, 90
- Inayoshi, K. & Maiolino, R. 2025, *ApJ*, 980, L27
- Ito, K., Valentino, F., Farcy, M., et al. 2025, arXiv e-prints, arXiv:2503.01953
- Jespersen, C. K., Cranmer, M., Melchior, P., et al. 2022, *ApJ*, 941, 7
- Jespersen, C. K., Melchior, P., Spergel, D. N., et al. 2025a, arXiv e-prints, arXiv:2503.03816
- Jespersen, C. K., Steinhardt, C. L., Somerville, R. S., & Lovell, C. C. 2025b, *ApJ*, 982, 23
- Jin, S., Sillassen, N. B., Magdis, G. E., et al. 2024, *A&A*, 683, L4
- Kakimoto, T., Tanaka, M., Onodera, M., et al. 2024, *ApJ*, 963, 49
- Koekemoer, A. M., Faber, S. M., Ferguson, H. C., et al. 2011, *ApJS*, 197, 36
- Kokorev, V., Caputi, K. I., Greene, J. E., et al. 2024a, *ApJ*, 968, 38
- Kokorev, V., Chisholm, J., Endsley, R., et al. 2024b, *ApJ*, 975, 178
- Kroupa, P. 2001, *MNRAS*, 322, 231
- Kugel, R., Schaye, J., Schaller, M., et al. 2023, *MNRAS*, 526, 6103
- Lacey, C. G., Baugh, C. M., Frenk, C. S., et al. 2016, *MNRAS*, 462, 3854
- Lagos, C. d. P., Bravo, M., Tobar, R., et al. 2024, *MNRAS*, 531, 3551
- Lagos, C. d. P., Tobar, R. J., Robotham, A. S. G., et al. 2018, *MNRAS*, 481, 3573
- Lagos, C. d. P., Valentino, F., Wright, R. J., et al. 2025, *MNRAS*, 536, 2324
- Langeroodi, D. & Hjorth, J. 2023, *ApJ*, 957, L27
- Langeroodi, D. & Hjorth, J. 2024, arXiv e-prints, arXiv:2404.13045
- Larson, R. B. 1974, *MNRAS*, 169, 229
- Leja, J., Carnall, A. C., Johnson, B. D., Conroy, C., & Speagle, J. S. 2019a, *ApJ*, 876, 3
- Leja, J., Johnson, B. D., Conroy, C., et al. 2019b, *ApJ*, 877, 140
- Leja, J., Speagle, J. S., Johnson, B. D., et al. 2020, *ApJ*, 893, 111
- Lim, S., Tacchella, S., Maiolino, R., Schaye, J., & Schaller, M. 2025, arXiv e-prints, arXiv:2504.02027
- Long, A. S., Antwi-Danso, J., Lambrides, E. L., et al. 2024, *ApJ*, 970, 68
- Looser, T. J., D'Eugenio, F., Maiolino, R., et al. 2024, *Nature*, 629, 53
- Lovell, C. C., Roper, W., Vijayan, A. P., et al. 2023, *MNRAS*, 525, 5520
- Madau, P. & Dickinson, M. 2014, *ARA&A*, 52, 415
- Man, A. & Belli, S. 2018, *Nature Astronomy*, 2, 695
- Marigo, P., Bressan, A., Nanni, A., Girardi, L., & Pumo, M. L. 2013, *MNRAS*, 434, 488
- Martig, M., Bournaud, F., Teyssier, R., & Dekel, A. 2009, *ApJ*, 707, 250
- Matthee, J., Naidu, R. P., Brammer, G., et al. 2024, *ApJ*, 963, 129
- McLeod, D. J., McLure, R. J., Dunlop, J. S., et al. 2021, *MNRAS*, 503, 4413
- Merlin, E., Fortuni, F., Torelli, M., et al. 2019, *MNRAS*, 490, 3309
- Mosleh, M., Riahi-Zamin, M., & Tacchella, S. 2025, arXiv e-prints, arXiv:2503.14591
- Moster, B. P., Somerville, R. S., Newman, J. A., & Rix, H.-W. 2011, *ApJ*, 731, 113
- Nanayakkara, T., Glazebrook, K., Jacobs, C., et al. 2024, *Scientific Reports*, 14, 3724
- Nanayakkara, T., Glazebrook, K., Schreiber, C., et al. 2025, *ApJ*, 981, 78
- Pascalau, R. G., D'Eugenio, F., Tacchella, S., et al. 2025, arXiv e-prints, arXiv:2505.06349
- Peng, Y., Maiolino, R., & Cochrane, R. 2015, *Nature*, 521, 192
- Peng, Y.-j., Lilly, S. J., Kovač, K., et al. 2010, *ApJ*, 721, 193
- Pillepich, A., Springel, V., Nelson, D., et al. 2018, *MNRAS*, 473, 4077
- Planck Collaboration, Aghanim, N., Akrami, Y., et al. 2020, *A&A*, 641, A6
- Puskás, D., Tacchella, S., Simmonds, C., et al. 2025, *MNRAS*, 533, 3222
- Rieke, M. J., Robertson, B., Tacchella, S., et al. 2023, *ApJS*, 269, 16
- Russell, T. A., Dobric, N., Adams, N. J., et al. 2024, arXiv e-prints, arXiv:2412.11861
- Sánchez-Blázquez, P., Peletier, R. F., Jiménez-Vicente, J., et al. 2006, *MNRAS*, 371, 703
- Santini, P., Castellano, M., Merlin, E., et al. 2021, *A&A*, 652, A30
- Schaye, J., Crain, R. A., Bower, R. G., et al. 2015, *MNRAS*, 446, 521
- Schaye, J., Kugel, R., Schaller, M., et al. 2023, *MNRAS*, 526, 4978
- Schechter, P. 1976, *ApJ*, 203, 297
- Schreiber, C., Glazebrook, K., Nanayakkara, T., et al. 2018, *A&A*, 618, A85
- Schreiber, C., Pannella, M., Elbaz, D., et al. 2015, *A&A*, 575, A74
- Shuntov, M., Ilbert, O., Toft, S., et al. 2025, *A&A*, 695, A20
- Silk, J. & Rees, M. J. 1998, *A&A*, 331, L1
- Skilling, J. 2004, in *American Institute of Physics Conference Series*, Vol. 735, Bayesian Inference and Maximum Entropy Methods in Science and Engineering: 24th International Workshop on Bayesian Inference and Maximum Entropy Methods in Science and Engineering, ed. R. Fischer, R. Preuss, & U. V. Toussaint (AIP), 395–405
- Somerville, R. S. & Davé, R. 2015, *ARA&A*, 53, 51
- Speagle, J. S. 2020, *MNRAS*, 493, 3132
- Springel, V., Pakmor, R., Pillepich, A., et al. 2018, *MNRAS*, 475, 676
- Steinhardt, C. L., Jespersen, C. K., & Linzer, N. B. 2021, *ApJ*, 923, 8
- Strait, V., Brammer, G., Muzzin, A., et al. 2023, *ApJ*, 949, L23
- Suess, K. A., Weaver, J. R., Price, S. H., et al. 2024, *ApJ*, 976, 101
- Tanaka, M., Valentino, F., Toft, S., et al. 2019, *ApJ*, 885, L34
- Taylor, M. B. 2005, in *Astronomical Society of the Pacific Conference Series*, Vol. 347, *Astronomical Data Analysis Software and Systems XIV*, ed. P. Shopbell, M. Britton, & R. Ebert, 29
- Trussler, J., Maiolino, R., Maraston, C., et al. 2020, *MNRAS*, 491, 5406
- Turner, C., Tacchella, S., D'Eugenio, F., et al. 2025, *MNRAS*, 537, 1826
- Urbano Stawinski, S. M., Cooper, M. C., Forrest, B., et al. 2024, *The Open Journal of Astrophysics*, 7, 46
- Valentino, F., Brammer, G., Gould, K. M. L., et al. 2023, *ApJ*, 947, 20
- Valentino, F., Heintz, K. E., Brammer, G., et al. 2025, arXiv e-prints, arXiv:2503.01990
- Veilleux, S., Cecil, G., & Bland-Hawthorn, J. 2005, *ARA&A*, 43, 769
- Vogelsberger, M., Marinacci, F., Torrey, P., & Puchwein, E. 2020, *Nature Reviews Physics*, 2, 42
- Weaver, J. R., Davidzon, I., Toft, S., et al. 2023, *A&A*, 677, A184
- Weaver, J. R., Taamoli, S., McPartland, C. J. R., et al. 2025, *A&A*, 697, A16
- Weibel, A., de Graaff, A., Setton, D. J., et al. 2024a, arXiv e-prints, arXiv:2409.03829
- Weibel, A., Oesch, P. A., Barrufet, L., et al. 2024b, *MNRAS*, 533, 1808
- Williams, C. C., Tacchella, S., Maseda, M. V., et al. 2023, *ApJS*, 268, 64
- Wu, P.-F. 2025, *ApJ*, 978, 131

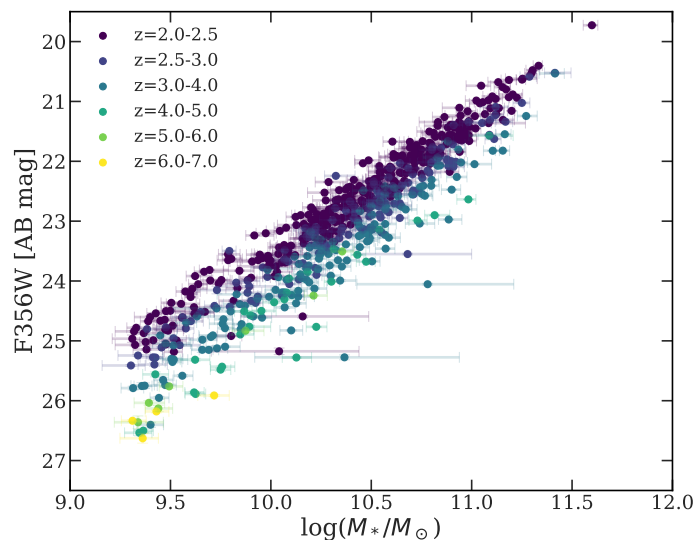


Fig. B.1. F356W magnitude versus stellar mass colour coded in bins of redshift for our sample.

Appendix A: BAGPIPES setup

Here we explain in more depth our BAGPIPES setup. We use the updated Bruzual & Charlot (2003) stellar population models (Chevalard & Charlot 2016) alongside the MILES library of stellar spectra (Sánchez-Blázquez et al. 2006; Falcón-Barroso et al. 2011) and the updated stellar tracks from Bressan et al. (2012); Marigo et al. (2013). Nebular components, i.e. line and continuum emission is incorporated following the procedure in Byler et al. (2017). We enable the ionization parameter U to vary between -4.5 and -0.5 in log space. We use a Calzetti et al. (2000) dust attenuation prescription with the dust extinction in the V band allowed to vary between 0-8 magnitudes.

For our star-formation history we use a parametric double power law prescription (Carnall et al. 2018, 2019b). There is much debate about how best to model high- z star-formation histories (see Carnall et al. 2019a; Leja et al. 2019a, for more of a review of the various methods). We chose a double power law model due to the increased speed in model fitting and since we are primarily fitting broad band photometry we are not particularly sensitive to the exact details of the star-formation history. It should be noted that differences in stellar masses are found when using a more flexible "continuity" SFH (Leja et al. 2019b), however it remains unclear whether the "continuity" prior used in the fitting is really physically motivated at high- z (see Turner et al. 2025; Mosleh et al. 2025). In light of this we stick with the more simple prescription. We use a uniform prior between 0.01 and 1000 for the indices α and β in the double powerlaw SFH. We leave stellar metallicity free to vary between -2.5 and 0.19 in log space (i.e. $\log(Z/Z_{\odot}) = (-2.5, 0.19)$), whilst noting that we cannot constrain this parameter from photometry. During our initial run we left the redshift free to vary and then compared the results for 18 spectroscopically confirmed galaxies from Baker et al. (2025b) (see Appendix E). We found that the EAZY redshifts were more accurate than the BAGPIPES redshifts so we fix the BAGPIPES redshifts to that of the EAZY values.

Appendix B: Completeness

Fig. B.1 shows the F356W magnitude versus stellar mass, colour coded by bins of redshift for our entire sample. The key takeaway is that due to our mass cut of $M_* > 10^{9.3} M_{\odot}$ for the SMFs and $M_* > 10^{10} M_{\odot}$ for the number densities we are able to see any massive quiescent galaxy within the survey area. The observed F356W magnitude versus stellar mass figure shows that, due to our mass cut, we are clearly complete and are not missing sources due to being magnitude limited. We also see an expected evolution with redshift with the higher redshift sources appearing fainter.

Appendix C: Stellar mass function fitting

The first aspect to note is that uncertainties on individual quantities of course end up affecting the SMF itself. For example, errors on redshifts and stellar masses resulting from SED modelling can lead galaxies to be in the wrong bins, which can be hard to diagnose since SED codes generally produce overconfident posteriors due to model misspecification Jespersen et al. (2025a). Therefore we consider typical uncertainties/biases derived from other studies. Generally photometric redshifts are measured accurately due to the number of bands and flexibility of templates, but there are offsets of 0.1-0.2dex (Baker et al. 2025b) (and see Appendix E). Stellar masses can have significant systematic offsets of up to 0.3dex (Conroy 2013).

In the actual measurements of the SMF, there are three common forms of error (e.g. Adams et al. 2021; Weaver et al. 2023; Shuntov et al. 2025). The first of these is completeness. For a photometric study such as this one this takes the form of the well-known Malmquist bias – we are limited in magnitude as to the faintest object we can see. In our case we have a mass cut of greater

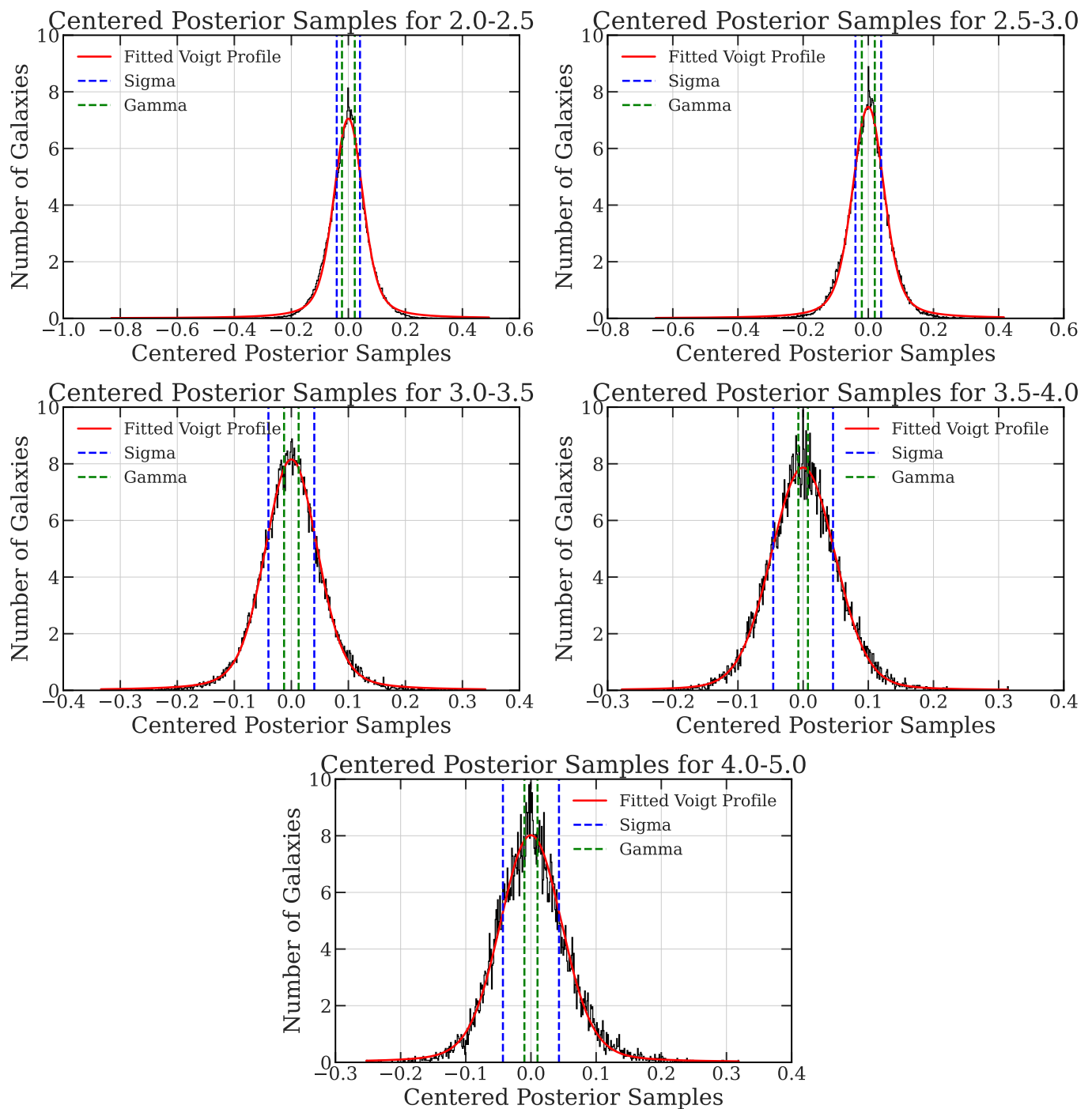


Fig. C.1. Density kernels produced by stacking the normalised stellar masses of all galaxies within each redshift bin. These are fit with a Voigt profile which is then convolved with the SMF for that redshift in order to account for [Eddington \(1913\)](#) bias.

than $M_{\star} > 10^{9.3} M_{\odot}$, and as can be seen in Appendix Fig B.1 our faintest object is far above our limiting magnitude. So for our purposes our sample is mass complete above $M_{\star} > 10^{9.3} M_{\odot}$.⁸

The second issue is cosmic variance. With deep extragalactic surveys we can only probe a small fraction of the sky hence our volume is necessarily limited. Whilst the Universe is likely homogeneous on large enough scales, we cannot probe those exact scales. We help minimise the effect of cosmic variance by using a large survey area (our area is approximately 6x the size of other comparable studies), but also by using fields in various different regions of the sky (as in [Valentino et al. 2023](#)). In computing our observational errors we use a prescription for fractional cosmic variance for each redshift and mass bin based on the approach of [Jespersen et al. \(2025b\)](#).

⁸ This is however a big issue when probing low-mass rapidly quenched galaxies ([Looser et al. 2024](#); [Baker et al. 2025a](#)) which are commonly missed due to their faintness ([Gelli et al. 2025](#); [Langeroodi & Hjorth 2024](#)).

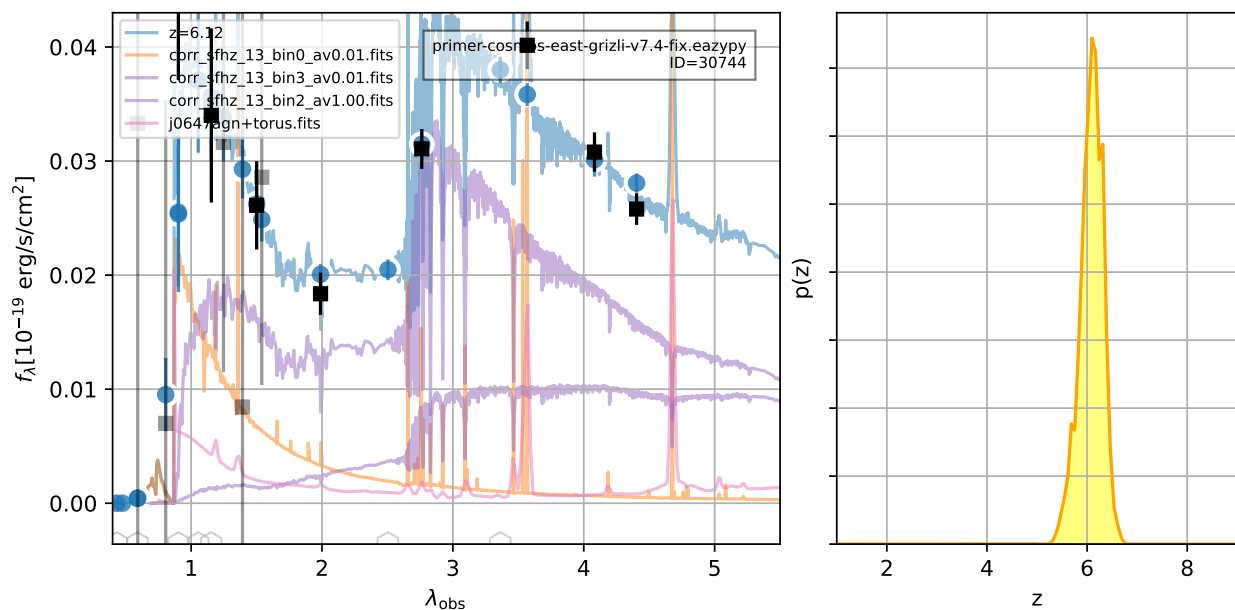


Fig. D.1. Left: Best-fit EAZY templates to 30744. We note that it has a MIRI detection which is not shown here. Right: the EAZY redshift posterior distribution for the source.

The final source is the so called "Eddington Bias" (Eddington 1913). This occurs due to measurement errors in quantities. For our work this almost entirely corresponds to the stellar mass of the galaxies. Due to the impossibility of knowing their masses exactly, galaxies can scatter to higher or lower masses than their "true" values. If the masses were equally distributed this would result in the same number of galaxies scattering to higher stellar masses as the number scattering to lower stellar masses. However, as can be seen in most papers exploring stellar mass functions (e.g. Davidzon et al. 2017; Adams et al. 2021; Weaver et al. 2023; Shuntov et al. 2025) there are more galaxies at certain masses than at others. This means that this scatter has a preferred direction, meaning this result must be accounted for when fitting a stellar mass function. This can be taken into account in multiple ways. The approach we will use is to take into account the posterior samples for each galaxy fit from BAGPIPES. We then fit a Voigt profile (a convolution of a Gaussian with a Lorentzian profile) to this normalised distribution to obtain a measure of the scatter. This Voigt profile is then convolved with the stellar mass function and the convolution of them both is fit to the data. It is also possible to create kernels based upon the posterior distributions (e.g. Shuntov et al. 2025), but we find that the Voigt profile fits our posterior distributions well (see Appendix Fig. C.1). An alternative approach is to use a likelihood based methodology when fitting (Leja et al. 2019b), but we do not use this approach in our work due to our smaller sample size.

Appendix D: EAZY fitting and posterior for high-z target

In this section we explore in more depth our selection for high-redshift candidates. This is the most challenging in terms of rooting out possible contaminants due to the combined contamination of both Brown Dwarves and LRDs. As mentioned earlier, Brown Dwarves are removed by a colour cut following the criteria of Langeroodi & Hjorth (2023) and Kokorev et al. (2024a) with any galaxy whose colour falls within the tracks of the modelled Brown Dwarves being removed. The effect of this cut is to remove galaxies with blue F150W-F200W and red F200W-F277W. However, we acknowledge with this method it is possible that Brown Dwarves still remain due to uncertainties in the blue bands of the photometry although we have done our best to mitigate this with the visual inspection.

LRD contamination remains more challenging as they would appear to be a combination of AGN and quiescent galaxies. We want the quiescent galaxies in our sample but do not want the (purely) AGN. At these redshifts almost all these sources are point-like so in some ways the difference between a LRD and a quiescent galaxy is a tricky question. Our approach is to remove galaxies based on visual inspection. We do not use any AGN templates in our BAGPIPES SED modelling (although note that this is possible, e.g. Carnall et al. 2023b), hence we remove galaxies that appear poorly fit, likely due to an AGN contribution to the continuum or other contamination effect. We also remove galaxies with a clear "V" shaped spectrum.

In Fig. D.1 we show the best fit EAZY model and the posterior for our high-z candidate 30744 which is found within the Primer Cosmos field. We see that the posterior is fully consistent with a redshift of around 6. We again note that this candidate has a MIRI detection which is not shown in the best-fit EAZY model.

Appendix E: Comparison to spectra

We can compare our SED fit quantities to other spectroscopic works in order to see how well we are able to recover quantities from photometry alone. We compare to the 18 massive quiescent galaxies from Baker et al. (2025b) who used both NIRSpect PRISM spectra and photometry in their SED modelling. The results of this is shown in Fig. E.1. We see that our photometric redshifts are

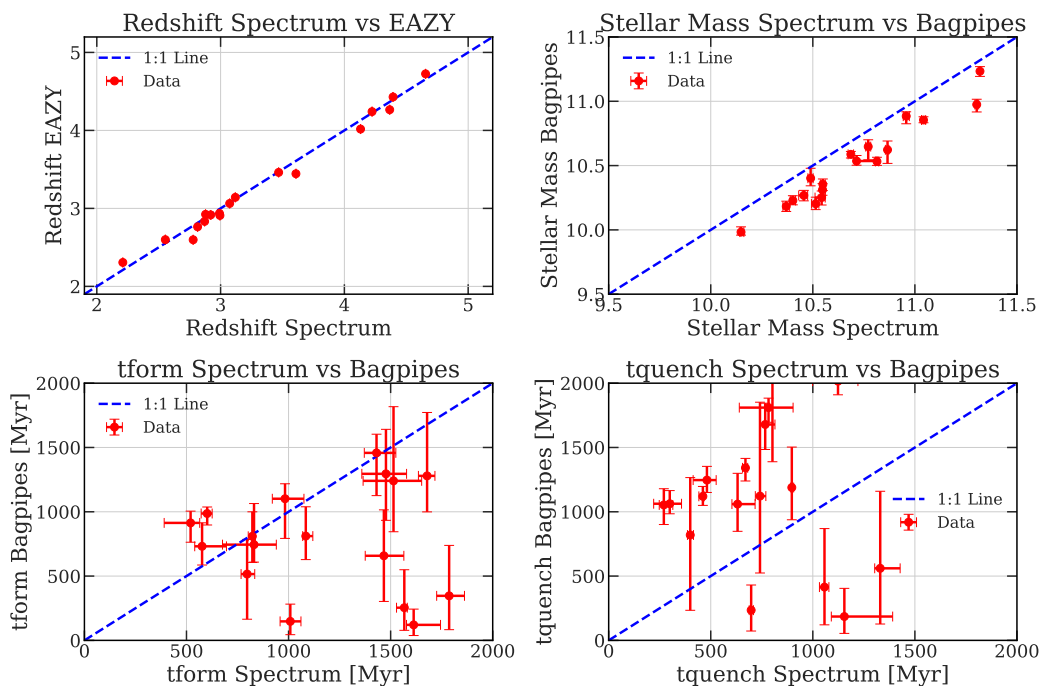


Fig. E.1. Comparison between quantities for a sample of 18 massive quiescent galaxies from Baker et al. (2025b) compared with our work. Upper left: comparison of our photometric EAZY redshifts versus the spectroscopic redshifts. Upper right, a comparison of the stellar masses, lower left, comparison of the formation times and lower right a comparison of the quenching time.

accurate for these galaxies with no significant offsets. Our stellar masses are slightly lower, but this is also likely due to the different SFHs between the Baker et al. (2025b) work and our own (for more details between offsets in SFHs see Leja et al. 2019a). However, we see clearly that we cannot accurately constrain formation or quenching times from photometry alone. This motivates further spectroscopic exploration of large samples of massive quiescent galaxies in order to understand their SFHs on a population level.